

Slip-Flow Regimes in Nanofluidics: A Universal Superexponential Model


Mohammad Aminpour^{1,2}, Sergio Andres Galindo Torres,^{3,4,*} Alexander Scheuermann,² and Ling Li^{3,4}

¹*Civil and Infrastructure Engineering Discipline, School of Engineering, RMIT University, Victoria 3001, Australia*

²*School of Civil Engineering, The University of Queensland, Brisbane, QLD 4072, Australia*

³*School of Engineering, Westlake University, Hangzhou 310024, China*

⁴*Key Laboratory of Coastal Environment and Resources of Zhejiang Province (KLaCER), School of Engineering, Westlake University, Hangzhou, China*

 (Received 1 October 2020; revised 22 March 2021; accepted 12 April 2021; published 24 May 2021)

Many experiments have shown large flow-enhancement ratios (up to 10^5) in carbon nanotubes (CNTs) with diameters larger than 5 nm. However, molecular-dynamics simulations have never replicated these results maintaining a 3-orders-of-magnitude gap with measurements. Our study provides a generic model of nanofluidics for continuum slip flow (diameter > 3 nm) that fills this significant gap and sheds light on its origin. Compared to 140 literature cases, the model explains the entire range of experimental flow enhancements by changes of nanotube diameters and finite variations of interfacial energies. Despite large variations of flow-enhancement ratios spanning 5 orders of magnitude in experimental results, the ratio between these data and corresponding model predictions approaches unity for the majority of experiments. The role of viscous entrance effects is discussed. The model provides insight into puzzling observations such as differences of CNTs and boron-nitride nanotubes, the slip on low-contact-angle surfaces and massive functionalization effects. This study could advance our understanding of nanoscale transport mechanisms and aid the design of tailored nanomembranes.

DOI: [10.1103/PhysRevApplied.15.054051](https://doi.org/10.1103/PhysRevApplied.15.054051)

I. INTRODUCTION

Incredibly fast flows observed in carbon nanotubes (CNTs) [1–5] have attracted much interest with potential applications in desalination, filtration, and energy conversion [6–9]. High flow rates attributed to the slip condition on interfaces lead to significant flow-enhancement ratios, ε (the ratio between observed and classically predicted flow rates).

However, the measured flow-enhancement ratios in nanotubes varied substantially ($\varepsilon = 1 - 10^6$). The controversy emerged from the early report of Majumder *et al.* [1] who experimented on nanotubes of larger diameters ($d = 7$ nm) than those of Holt *et al.* [2] ($d = 1.6$ nm) and yet measured greater flow enhancements than the latter by 1 to 2 orders of magnitude. Molecular-dynamics (MD) simulations supported only a portion of experimental results, mainly in a subcontinuum flow regime, typically for $d < 1.66$ nm [10,11]. The simulations failed to explain the observed very intensive flow enhancements with $\varepsilon = 10^3 - 10^5$ in larger nanotubes ($d > 5$ nm), although they were independently reported in several experiments [1,3,5,12–17]. The disagreement (a 3-orders-of-magnitude underprediction of

ε by MD simulations) led to scepticism on the accuracy of the measurements [18–20]. On the other hand, unambiguous measurements of water flow in individual CNTs provided further evidence of significant flow enhancements in relatively large tubes ($d = 30$ – 100 nm) [3]. With the measured flow rates far exceeding the numerical predictions, Secchi *et al.* posed more challenges on the MD simulations [3]. Moreover, observing no flow enhancement for boron-nitride nanotubes (BNNTs), which are crystallographically similar to CNTs, led to further complication concerning the slip-flow behavior [3]. The insufficiency of MD models to identify the differences between CNTs and BNNTs [21,22] or to estimate the scales of such differences due to corrugation effects [23,24], motivated the authors of Ref. [3] to link the phenomenon to physiochemical factors, in a perspective beyond hydrodynamic theories. Overall, a 3-orders-of-magnitude mismatch has remained unresolved between the MD predictions and experimental results of nanotube flow enhancements [25].

The range of MD (Lennard-Jones) intermolecular potentials are truncated at 1 nm. The mechanisms beyond van der Waals (vdW) interactions including longer-ranged water molecule orientation, correlations in the hydrogen-bonding network or proton hopping are poorly understood and too complex to be thoroughly simulated

*s.torres@westlake.edu.cn

via MD models. However, supported by substantial experimental evidence, the *pure* hydrophobic forces are much stronger and longer-ranged than the Lifshitz vdW force [26–28]. Furthermore, small perturbations in carbon-water interactions could have drastic impacts on the nanotube transmissivity [11], but no comprehensive study is yet performed.

A single-file or ring-style subcontinuum molecular mechanism for the narrowest nanotubes ($d < 1.66$ nm) [10,11], and also the curvature effects are hypothesized as the origin of nanotube ultraconductivity [19]; however, none has explained high flow enhancements observed in larger nanotubes ($d > 5$ nm) [1,3,5,12–17].

A few theoretical models have been proposed in search of a generalized slip-flow model in nanoscales [29,30]. These models are based on limited MD data, which are correlated linearly for estimating critical parameters, e.g., slip lengths and viscosity. The contact angle, θ is normally used to quantify interfacial effects, however, it does not fully reflect the surface hydrophobicity [31] and is insufficient in reproducing MD interaction parameters [32]. Furthermore, these models link high flow enhancements to large θ ($> 150^\circ$), which is incompatible with the moderately hydrophobic nature of CNTs (with reported $\theta_{\text{graphene}} \approx 70^\circ\text{--}90^\circ$ [33–36], and $\theta_{\text{CNT}} \approx 70^\circ$ [37]). Modifying classical hydrodynamics, another theory has corrected enhancement ratios from an order of 10^3 to unity with some experimental data examined [38].

Indeed, experiments [1,3,12,13] and MD simulations [18–20] have been challenging each other over the last 15 years. A clear-cut model or theory for nanofluidic slip flow is yet to be achieved. Here using a continuum approach—proven to be valid for nanofluidics [10,39,40]—incorporated with interface intermolecular potentials, we present a universal model of nanoscale continuum fluid transport for nanotubes and nanochannels. The model applies to the continuum regime where channel width $d > 3$ nm and channel lengths are practically long in which entrance effects are not dominant. In our model, a single dimensionless number uniquely characterizes the flow behavior, i.e., flow-rate-enhancement ratios (slip lengths). The model successfully explains the entire range of continuum-flow experimental data including those unpredictable by previous MD simulations. This model explains the large experimental data scatters by changes in nanotube diameters where small perturbations or chemical variations of interface properties are also discussed. Our study also sheds light on the origin of a significant mismatch between MD simulations and experiments by incorporating the actual interfacial energy levels. We also discuss the significance of viscous entrance effects.

Our method being already examined on complex and slip-flow regimes [41,42], bypasses the limitations of computationally expensive MD models (in simulating larger dimensions, parametric sensitivity analyses, accurate force

fields, and complicated interplay of molecular features). Hence, the approach allows us to provide a more complete picture of flow behavior in response to parametric variations, i.e., interfacial effects (energies) and the system’s characteristic length scales. We also investigate the influence of different interfacial force functions and variations of their effective lengths to test the generality of the proposed slip-flow model (see Appendix A for the details).

II. MODELING INTERFACE INTERMOLECULAR INTERACTIONS

To consider the averaged intermolecular mechanism involved in nanoscale fluid slippage, we develop a numerical approach incorporated with well-established interaction potentials for interfaces based on nanoscale experiments [26,28]. The approach is potentially capable of including additional longer-range interactions not included in the combination of electrostatic double layer and vdW theories [28,31]. A general interaction potential that best describes the hydrophobic interactions is developed as an exponential function of the effective interfacial energy γ_i^{eff} (positive for hydrophobic interfaces and negative for hydrophilic—hydrated—ones) [28,43,44] with a decay length of approximately equal to 0.3–2 nm [28]. For fully hydrophobic surfaces, γ_i^{eff} is equivalent to γ_i . For graphene as the substance for making CNTs, the (effective) interfacial energy in water is directly measured to be $\gamma_{i(\text{graphene})} = 83 \pm 7$ mJ/m² [34] with also similar values reported experimentally (90 mJ/m²) [45] and numerically (94–99 mJ/m²) [46] (see Table II for a review).

Unlike the hydrophobic interactions, the hydrophilic ones are not well defined in terms of interfacial energy. Negative interfacial energy means a tendency of the interface to expand indefinitely, i.e., miscible media resulting in eventually dissolved interfaces with γ_i approaching 0, thus thermodynamically unstable. However, the interface may be kept in place by attractive physical interactions or chemical bonds to substrates (crystallization or strong covalent crosslinking) [28,31,43]. Negative γ_i^{eff} accounts for solid-fluid attractive effects in hydrophilic interfaces with effective hydration forces resulting from the water ability to hydrogen bond and hydrate the surface. For a hydrophilic surface, observed effective interfacial energies are in the range of $\gamma_i^{\text{eff}} = -0.5$ to -15 mJ/m² (e.g., -2.5 for silica surfaces in water, and -0.5 to -5 mJ/m² for mica in different cation salt solutions), with the theoretical limit of the surface tension of water ($\gamma_l = 72.8$ mJ/m² for water at 20 °C) [28].

Here, we develop an exponentially decaying (hydrophobic or hydrophilic) solid-fluid intermolecular force function, $\mathbf{F}_h(y) = -\rho(y)\mathbf{g}_h = -\rho(y)\mathbf{g}_{h_0}e^{-y/l_s}$, where $\rho(y)$ is the fluid density, y is the normal distance from the wall, \mathbf{g}_{h_0} is the force strength factor (in units of acceleration),

and s is the decay length [see Fig. 1(a)]. Such forces generate interfacial energies γ_i^{eff} [see Fig. 1(b)] calculated from simulations as the integration of pressure differences (see Appendix A for methods). Upscaling the molecular-scale properties, e.g., depletion and adsorption molecular layering, this model facilitates the simulation of fundamental vdW forces and the longer-ranged effects. While the origin and exact molecular mechanisms of these forces remain unknown [31], we retrieve their resultant effects—in scales of interfaces—and match it with accurately measured data in terms of γ_i^{eff} in nanoscopic experiments. We also show that the conclusions are independent of the solid-fluid force functions (exponential or constant) and the ranges of forces (short or long range), but mainly dependent on incorporating accurate interfacial energy levels (see Appendix A 7).

Here, the definition of hydrophobic or hydrophilic surfaces is based on positive or negative γ_i , which is different from a sole θ criterion. γ_i is directly related to the solid-surface energy, γ_s and θ via Young's equation [48]:

$$\gamma_i = \gamma_s - \gamma_l \cos \theta, \quad (1)$$

where γ_l is the fluid surface tension.

Our model is developed based on continuum simulations with surface-water interfacial interactions modeled using up-layer averaged molecular potentials. While averaging fluid layering at the interface, the model averages molecular interactions including corrugations with their effects as variations in interfacial fluid density and viscosity. Also as shown in Ref. [49], both corrugation and fluid-solid interactions are affecting the slip where the responsible molecular signature appears to be the distribution of water molecules within the contact layer, coupled with the strength of water-surface interactions. This work also showed that the contact angle can change by variations of either lattice parameter or electrostatic parameter. Therefore, a change in corrugation can induce a variation in the macroscopic contact angle, despite the same intermolecular interaction parameters. One may then suggest that the average wetting property may inherently include the effects of corrugation when an up-layer averaging is maintained in simulations. Thus we suggest that the corrugation effects can be assumed as being implicitly included in our model.

III. FLOW RATE VARIATIONS AND MECHANISMS

The model predicts flow attenuation and enhancements (for hydrophilic and hydrophobic interfaces, respectively), indicated as deviations of the velocity profiles from the results under the no-slip assumption [Fig. 1(e)]. Deviated velocity profiles extrapolate into (apparent) negative and

positive slip lengths (λ), for hydrophilic and hydrophobic walls, respectively [Fig. 1(f)]. With larger slip lengths, fluid velocities tend to pluglike profiles [Fig. 1(e)], as also demonstrated in MD simulations [24,47].

The mechanism of such flow slippage (or inhibition) is attributed to fluid rarefaction (or densification) at interfacial layers next to hydrophobic (or hydrophilic) surfaces [Fig. 1(c)] extending to long-ranged molecule arrangements and hydrogen bonding incorporated with low (or high) fluid viscosity in the interface region. Such interfacial properties are supported by MD investigations demonstrating water depletion (and adsorption) next to hydrophobic (and less hydrophobic, i.e., low-contact-angle) surfaces [50,51]. Furthermore, the thermodynamically driven low-density depletion regions on hydrophobic interfaces are shown by x -ray reflectivity measurements with the thickness in the order of water molecules (2–4 Å), disappearing with decreased hydrophobicity [52,53]. Similar to our results, velocity jumps in the depletion region are computationally identified next to the hydrophobic CNT walls [24,47].

IV. A UNIVERSAL NANOFLUIDIC SLIP-FLOW MODEL

Considering the balance of the involved hydrodynamic forces in nanofluidics and the interfacial length scale, we define the *slip-flow number*. While the ratio of inertial to viscous forces, as indicated by Reynolds number, is the fundamental number representing hydrodynamic forces involved in the fluid-flow behavior, with scales approaching nanometers, interfacial forces can also become considerable as the fluid slip at interfaces can be significant. The interfacial tension (although a static force) is the parameter associated with the viscosity at the interfacial fluid layer. The viscosity is also directly linked with the interfacial friction at the slip layer in nanoscales. The capillary number, which is the ratio between viscous to interfacial forces, is then the potential representative number in these scales. Thus the ratio between Reynolds to capillary numbers as the balance of all forces multiplied by a function of the interfacial layer scale factor, i.e., $f(s/d)$ is used to define the slip-flow number Ω ,

$$\Omega = \frac{\text{Re}}{\text{Ca}} f\left(\frac{s}{d}\right) = \frac{\rho u d / \mu}{\mu u / \gamma_i^{\text{eff}}} f\left(\frac{s}{d}\right) = \frac{\rho \gamma_i^{\text{eff}} d}{\mu^2} f\left(\frac{s}{d}\right), \quad (2)$$

where ρ is the fluid (bulk) density, u is the fluid (average) velocity, d is the characteristic dimension of the system, e.g., tube diameter, μ is the dynamic viscosity for the bulk fluid, and s is the interfacial fluid-layer characteristic thickness ($s \approx 0.5$ nm). This number is based on the bulk values of density and viscosity but accounts for the subinterface

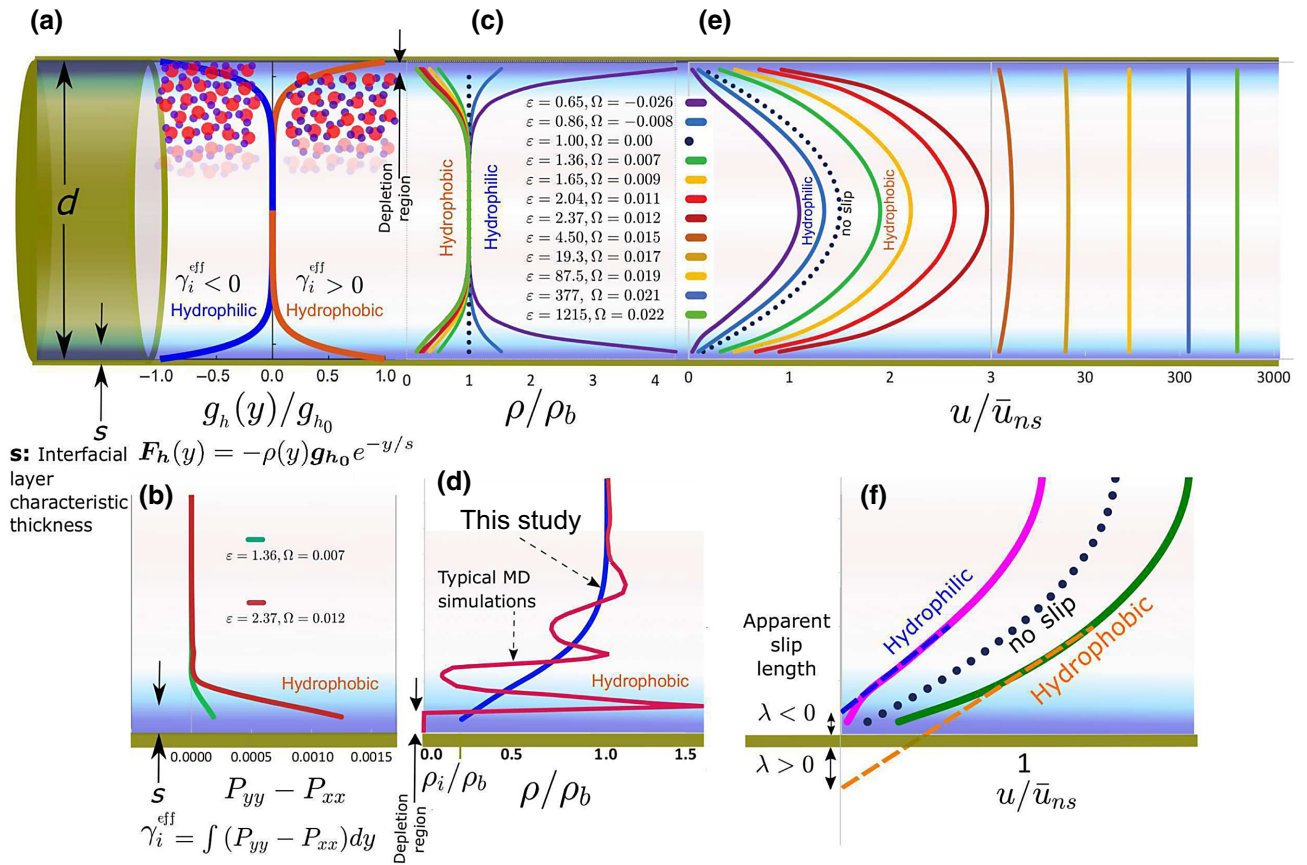


FIG. 1. Modeling slip-flow characteristics in nanotubes. (a) Intermolecular effects (combined vdW forces and effects beyond) are modeled using an interaction potential with an exponentially decaying, positive (hydrophobic) or negative (hydrophilic) force, corresponding to positive or negative γ_i^{eff} , respectively. The decay length of the force, s (approximately equal to 0.5 nm) is the characteristic thickness of the interfacial fluid layer. (b) γ_i^{eff} is calculated as the integrated difference of pressure components. (c) The density variations (normalized by the bulk density, ρ_b) correspond to the dimensionless *slip-flow number*, Ω and the flow-enhancement ratio, ϵ . (d) Capable of incorporating the molecular effects in ranges longer than MD models, our approach retrieves the interface hydrodynamic features, e.g., slip velocities while upscaling the depletion and adsorption molecular layering. (e) Enhanced and attenuated velocity profiles correspond to (f) positive and negative apparent slip lengths, respectively. The velocity jump takes place at the interfacial layer as also demonstrated by MD simulations [24,47], leading to pluglike velocity profiles at higher flow-enhancement ratios.

variations of these quantities intrinsically via the interfacial energy. When selecting the simulation scales, care has been taken to ensure that the validity of these considerations is not affected by a nonlocal viscosity [54]. We then assume a simple power function for f as $(s/d)^\alpha$.

A large number of pressure-driven flow systems (infinitely long tubes and parallel plates with different diameters and distances) are simulated where interfacial forces are varied from weak to strong, attractive to repulsive modes (in total more than 660 simulation cases including 22 tube and channel sizes each simulated for more than 30 different interfacial force conditions). Analyses of the results show that when $\alpha = 1.2$, all the $\Omega - \epsilon$ curves (for all systems examined) converge into a unique behavior (with the smallest sum of squared differences among the curves; see Appendix A 4 for more details). Thus we propose the dimensionless *slip-flow number* in the following

specific form:

$$\Omega = \frac{\rho\gamma_i^{\text{eff}}s}{\mu^2} \left(\frac{s}{d}\right)^{0.2}. \quad (3)$$

The characteristic length, d is readily the inner diameter of circular tubes including the depletion thickness. For nanochannels, we implement a geometrical transformation of the parallel plates into analogous tubes with identical solid-fluid interface area and volume of fluid that leads to $d = 2l$ where l is the separation distance of the plates. With such a transformation, consistent behavior is found for slip flows in tubes and between parallel plates when characterized by the same definition of *slip-flow number*.

To examine the generality of the model, we also test variations of the force models (with constant or exponentially decaying solid-fluid force functions with different

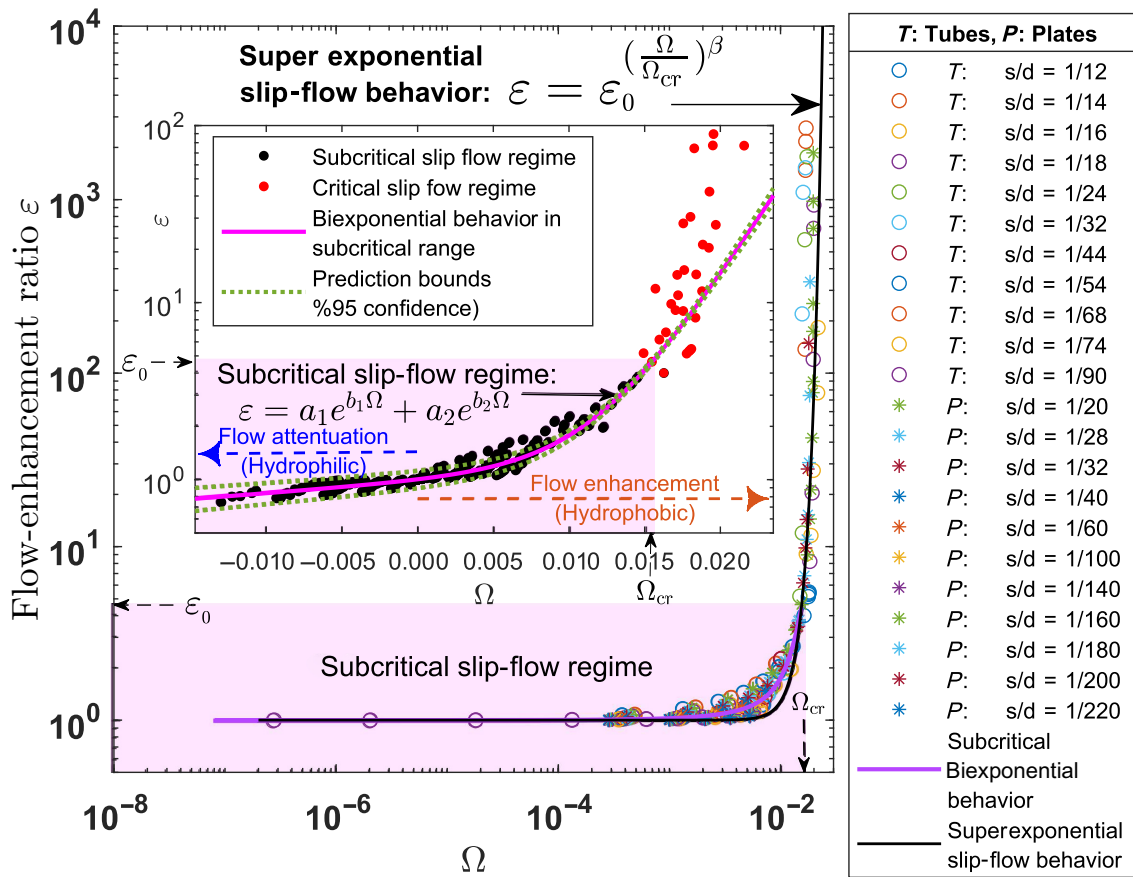


FIG. 2. The universal nanofluidic slip-flow model. The unified $\Omega - \varepsilon$ relationship provides a universal slip-flow model for nanofluidics (obtained for tubes and parallel plates). The model is presented as a superexponential function [Eq. (4): $\varepsilon = \varepsilon_0 (\Omega/\Omega_{cr})^\beta$] for the critical regime ($\Omega > \Omega_{cr}$) with the optimal coefficients' values: $\varepsilon_0 = 4.50$, $\Omega_{cr} = 0.0154$, and $\beta = 4.13$. A biexponential function can best describe the subcritical regime corresponding to flow attenuation and enhancement due to hydrophilic and hydrophobic effects, respectively (the inset).

decay lengths). Four different force functions are examined on three tube diameters, each simulated over more than 20 different force strengths (more than 240 cases in total). The analysis showed that the conclusions are universal with the same behavior observed at similar *slip-flow numbers* (see Appendix A 7 for more details).

As shown in Fig. 2, our simulations reveal a subcritical slip-flow behavior followed by a critical regime. The critical regime can be described by the following universal superexponential slip-flow function:

$$\varepsilon = \varepsilon_0 \left(\frac{\Omega}{\Omega_{cr}}\right)^\beta, \quad (4)$$

with $\varepsilon_0 \approx 4.50$, $\Omega_{cr} \approx 0.0154$, and $\beta \approx 4.13$. In this model, ε_0 is the flow-enhancement ratio corresponding to the threshold of critical behavior (the critical *slip-flow number*, Ω_{cr}) beyond which the slip flow turns into the critical superexponential regime, i.e., approaching the limit of frictionless walls.

For $\Omega < \Omega_{cr}$ (subcritical), the slip-flow regime is best characterized as a biexponential behavior, with the

following equation:

$$\varepsilon = a_1 e^{b_1 \Omega} + a_2 e^{b_2 \Omega}, \quad (5)$$

where the coefficients (with %95 confidence bounds) are $a_1 = 0.97$ (0.962, 0.987), $b_1 = 15.14$ (12.14, 18.15), $a_2 = 0.03$ (0.024, 0.037), and $b_2 = 304$ (290.6, 317.5). The subcritical regime describes both flow attenuation for hydrophilic ($\Omega < 0$) and flow enhancement for hydrophobic ($\Omega > 0$) cases up to $\Omega \approx \Omega_{cr}$ (Fig. 2, inset)

The normalized apparent slip lengths can also be shown as a function of Ω via the analytical relationship for tubes, $\varepsilon = 1 + 8(\lambda/d)$ (Fig. 3). The interfacial density, ρ_i , i.e., the average fluid density in the interface region next to walls (with characteristic thickness of $s \approx 0.5$ nm) is also shown to be a function of the nondimensionalized effective interfacial energy, $\gamma_i^{\text{eff}} = \{\gamma_i^{\text{eff}}/[\mu^2/(\rho s)]\}$ in Fig. 3. The value ρ_i/ρ_b (where ρ_b is the bulk density) indicates the range of fluid densification (and rarefaction) near hydrophilic (and hydrophobic) surfaces. A strong hydrophilicity (e.g., $\gamma_i^{\text{eff}} = -15$ mJ/m²) corresponding to $\gamma_i^{\text{eff}} = -0.0074$ can

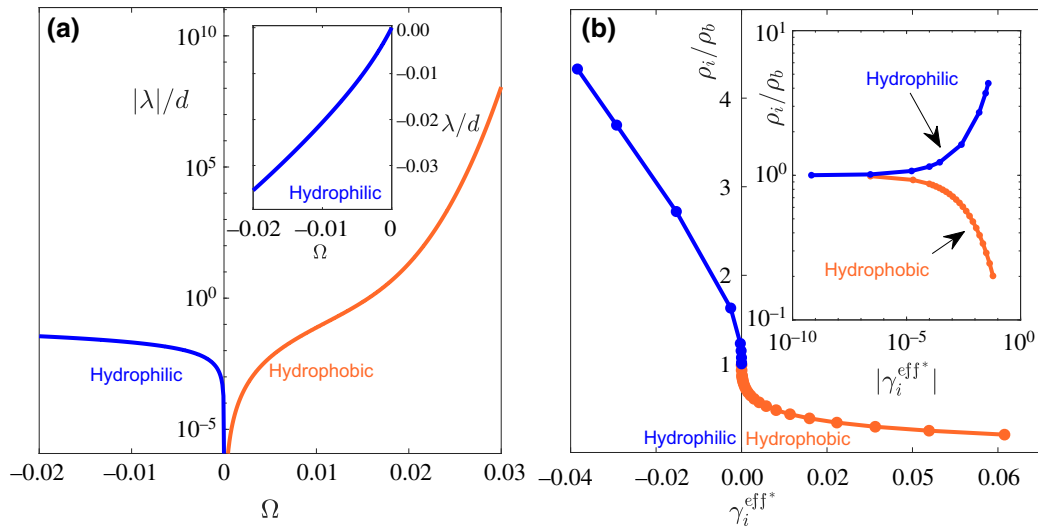


FIG. 3. The unified nanofluidic slip-flow characteristics. (a) The normalized apparent slip length as a function of Ω . Note the absolute value $|\lambda|$ in the graph. The inset shows the hydrophilic side of the graph with a normal scale for the vertical axis showing the actual negative values of λ/d . (b) Normalized average fluid density at the interfacial layer (ρ_i/ρ_b) versus the dimensionless effective interfacial energy ($\gamma_i^{\text{eff}*} = \frac{\gamma_i^{\text{eff}}}{\mu^2/(\rho_s)}$). The inset in (b) shows the density variations with a logarithmic vertical axis. Note the absolute value $|\gamma_i^{\text{eff}*}|$ used in the inset.

lead to water densification in the interface with $\rho_i/\rho_b \approx 2.05$. This densification is supported by experimental evidences such as the nanoacoustic measurements of a 5-times higher water density at Al_2O_3 hydrophilic surfaces in water (tending to bulk density in about 1-nm distance) [55]. Contrarily, a typical $\gamma_i = 83 \text{ mJ/m}^2$ for hydrophobic CNTs [34] gives $\gamma_i^{\text{eff}*} = 0.041$, which corresponds to the rarefaction at the interface ($\rho_i/\rho_b \approx 0.25$).

V. EXPERIMENTAL VALIDATION

A. Experimental estimation of the interfacial energy, γ_i for nanotube materials

Wetting properties of the nanotubes and their constituent materials were investigated in several previous studies as summarized in Table II. We select the following values as the interfacial energies of nanotube materials when calculating the Ω : $\gamma_{i(\text{CNT:graphene})} = 83 \text{ mJ/m}^2$ [34], $\gamma_{i(\text{BNNT})} = 23 \text{ mJ/m}^2$ [56], $\gamma_{i(\text{polysulfone UF})} = 48.93 \text{ mJ/m}^2$ [57], $\gamma_{i(\text{polycarbonate})} = 38.0 \text{ mJ/m}^2$ [58]. Particularly, we select the value of $\gamma_{i(\text{CNT:graphene})}$ from Ref. [34] in which the interfacial energy of graphene is directly measured using a surface force apparatus independently instead of an indirect estimation from other parameters (contact angle). The role of energy perturbations or functionalization effects are discussed later (Fig. 8).

B. Model validation

We compare our model with a large number of experimental data to evaluate the validity of the revealed

behavior (Fig. 4). The model is proposed for the continuum-flow regime up to the limit of the validity of classical hydrodynamics which can be up to a channel width of about ten molecular diameters, i.e., $d > 3 \text{ nm}$ [59,60]. The subcontinuum experiments indicate an evidently different behavior. We note that in the experiments conducted on outer-wall membranes by Lee *et al.* [16], the flow channels have been the voids between outer walls of vertical CNTs, not inside tubes. These untypical conditions may explain larger differences between these data and the model predictions. The details of experiments are summarized in Table I.

A comparison between our predicted enhancement ratios and experimental values as shown in Fig. 5(a) demonstrates a close agreement between the model and experiments across the entire range of ε variations. The ratio between experimental ε and corresponding predicted ones approaches unity for the majority of continuum experiments [Fig. 5(b)].

The model features the onset of the critical regime (Ω_{cr}) where flow enhancement intensifies superexponentially with Ω (Fig. 2). Both the critical regime's onset and the growth rates are evidently in agreement with the experimental data (Fig. 4).

To further examine the validity of this model, we independently derive the main features of the model from experiments, i.e., (a) the onset of the critical regime (Ω_{cr}) and (b) the superexponential growth rate. Firstly, we show that a range of $0.012 < \Omega_{\text{cr}} < 0.025$ for the proposed superexponential model ($\varepsilon = \varepsilon_0^{(\Omega/\Omega_{\text{cr}})^\beta}$, $\varepsilon_0 = 4.5$, $\beta = 4.13$) can cover %95 of experimental data from 41

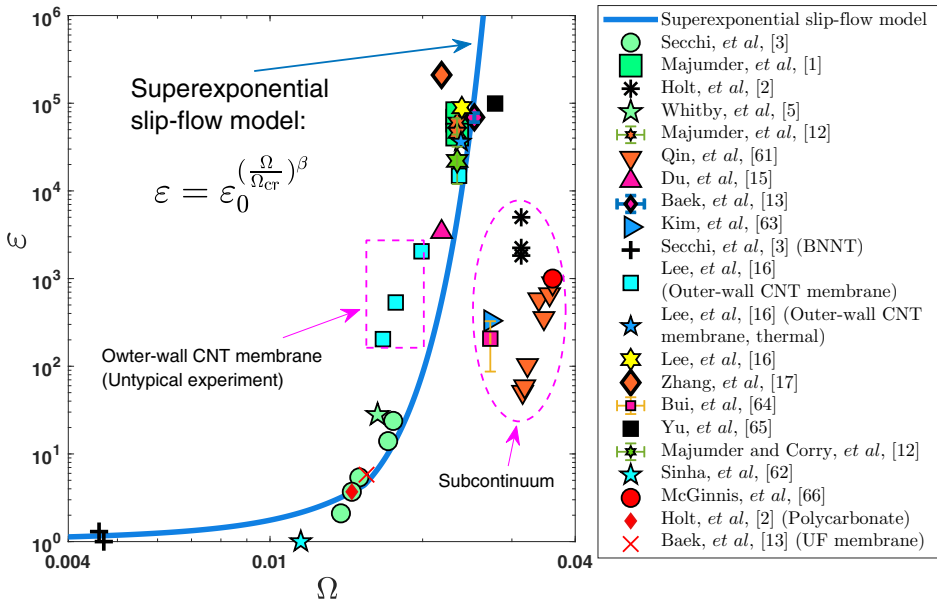


FIG. 4. The universal nanofluidic slip-flow model versus experimental data. Data extracted from 40 experiments on water flow in nanotubes are shown in comparison with the proposed universal slip-flow model (see Table I for experimental details). Note that the model is proposed for continuum slip-flow regime and the subcontinuum data are shown for comparison. Also note untypical conditions in outer-wall membranes where the voids between vertical close-ended tubes are used as flow channels. Also see Fig. 8.

experiments including the limiting subcontinuum data. The computationally determined value of $\Omega_{cr} = 0.0154$ developed for continuum regime lies within the given range derived from experimental data [see Fig. 6(a)]. Secondly, we independently investigate the growth rate of ε in experiments. For this purpose, we select those reports in which multiple tests were performed on nanotubes of different diameters. Thus, Ω in each set of these experiments varies with only diameters (with other materials and test conditions being constant). Therefore the growth rate of ε versus Ω in those experiments is a pure experimental outcome independent from any other assumption. As illustrated in Fig. 6(b), this analysis further validates the proposed superexponential growth model with the experimentally fitted value of β equal to 5.349 close to the computationally derived value of 4.13 for superexponential coefficient in our model (β in $\varepsilon = \varepsilon_0^{(\Omega/\Omega_{cr})^\beta}$).

VI. DISCUSSION

A. Entrance effects

The transition from a macroscopic reservoir to a nanoscale pore with streamlines being bent while entering the channel is a source of viscous dissipation. Considering a nanopore of radius R from which the flow enters a channel (tube) of the same radius, we can assume that the total hydrodynamic resistance \mathcal{R}_{pc} is the sum of the resistances through pore and channel, i.e., $\mathcal{R}_{pc} = \mathcal{R}_p + \mathcal{R}_c$. The total pressure drop ΔP is also the sum of pressure drops through pore and channel, $\Delta P = \Delta P_p + \Delta P_c$. Also the flow of the channel is $Q_c = \Delta P_c / \mathcal{R}_c$ while the flow through the pore is $Q_p = \Delta P_p / \mathcal{R}_p$. The entrance-corrected flow is then $Q_{pc} = Q_p = Q_c = \Delta P / (\mathcal{R}_c + \mathcal{R}_p)$.

For a nanopore, the flow rate can be written as

$$Q_p = \frac{R^3}{3\mu} \Delta P_p. \quad (6)$$

The flow rate through a pore is not significantly affected by slip conditions since the dissipation source is mainly geometric.

For the no-slip boundary conditions, it can be shown that entrance effects are apparently negligible for tube lengths exceeding a few channel radii [67].

Considering a nonzero slip length λ , the flow rate through a tube (channel) is given as

$$Q_c = \frac{\pi R^4}{8\mu L} \left(1 + \frac{4\lambda}{R} \right) \Delta P_c. \quad (7)$$

Therefore, the entrance-corrected flow rate in case of slip is

$$Q_{pc} = \frac{R^3}{3\mu} \frac{\Delta P}{1 + \frac{8L}{3\pi(R+4\lambda)}}. \quad (8)$$

From the above equation it can be seen that when $\lambda > R$, the hydrodynamic resistance is dominated by entrance effects as long as $\lambda > L$.

We use the value of $\mathcal{R}_p / \mathcal{R}_c = 3\pi(R/L + 4\lambda/L)/8$ as a criterion for the significance of entrance effects. Figure 7 shows this criterion in which the limit of $\mathcal{R}_p / \mathcal{R}_c > 1$ can be defined as the threshold of the flow being dominated by viscous entrance effects. With slip length λ reaching the order of channel length L , flow behavior approaches such a threshold [67].

Our model, which is based on channel slip flow in the continuum regime, is limited to relatively long tubes

TABLE I. Experimental data from the literature on water flow in nanomembranes versus our predictions. Here, for the calculation of $\Omega = (\rho\gamma_i s/\mu^2)(s/d)^{0.2}$, the following parameters are assigned: $\rho = 997 \text{ kg/m}^3$, $s = 0.5 \text{ nm}$, $\mu = 1.002 \text{ mPa s}$, $\gamma_{(\text{CNT-graphene})} = 83 \text{ mJ/m}^2$ [34], $\gamma_{(\text{BNNT})} = 23 \text{ mJ/m}^2$ [56], $\gamma_{(\text{polystyrene UF})} = 48.93 \text{ mJ/m}^2$ [57], and $\gamma_{(\text{polycarbonate})} = 38.0 \text{ mJ/m}^2$ [58]. The values are selected based on the review summary provided in Table II.

No.	Ref.	Material	d (nm)	CNT length, L (μm)	ϵ , Experiment	Slip length, λ (nm)	Ω	$\epsilon_{\text{our model}}$	$\mathcal{R}_p/\mathcal{R}_c$
1	Holt <i>et al.</i> [2]	CNT	1.65	2	5000.0	1031.0	0.0325	Subcontinuum	2.43
2	Holt <i>et al.</i> [2]	CNT	1.65	3	2240.0	461.8	0.0325	Subcontinuum	0.73
3	Holt <i>et al.</i> [2]	CNT	1.65	2.8	1830.0	377.2	0.0325	Subcontinuum	0.64
4	Holt <i>et al.</i> [2]	Polycarbonate	2.10	6	3.7	0.7	0.0145	Subcontinuum	0.00
5	Majumder <i>et al.</i> [1]	CNT	7	34	63333.3	55415.8	0.0243	19807.4	7.68
6	Majumder <i>et al.</i> [1]	CNT	7	34	77017.5	67389.5	0.0243	19807.4	9.34
7	Majumder <i>et al.</i> [1]	CNT	7	126	43859.6	38376.3	0.0243	19807.4	1.44
8	Secchi <i>et al.</i> [3]	CNT	30	0.7	23.8	85.3	0.0182	20.1	1.19
9	Secchi <i>et al.</i> [3]	CNT	34	0.45	14.0	55.2	0.0177	14.5	0.97
10	Secchi <i>et al.</i> [3]	CNT	66	0.9	5.4	36.1	0.0156	4.9	1.11
11	Secchi <i>et al.</i> [3]	CNT	76	0.8	3.7	25.3	0.0150	3.9	0.96
12	Secchi <i>et al.</i> [3]	CNT	100	1	2.1	14.0	0.0143	3.5	0.60
13	Secchi <i>et al.</i> [3]	BNNT	46	0.6	1.0	0.0	0.0049	1.2	0.85
14	Secchi <i>et al.</i> [3]	BNNT	52	0.7	1.3	2.0	0.0048	1.2	1.11
15	Whitby <i>et al.</i> [5]	CNT	43 \pm 3	78	28 \pm 6	145.1 \pm 32.3	0.0169	9.1	3.08
16	Majumder and Corry [12]	CNT	7	100	22000 \pm 10000	19249 \pm 8750	0.0243	19807.4	1.11
17	Majumder <i>et al.</i> [14]	CNT	7	34–126	60000 \pm 16000	52499 \pm 14000	0.0243	19807.4	3.03
18	Majumder <i>et al.</i> [14]	CNT	7	81	46000 \pm 21000	40249 \pm 18375	0.0243	19807.4	2.32
19	Majumder <i>et al.</i> [14]	CNT:	7	34–126	200 \pm 30	174 \pm 26	—	No info on γ_i	—
20	Majumder <i>et al.</i> [14]	tip-functionalized with a polypeptide spacer and the anionically charged dye molecule. CNT: tip and core-functionalized with a polypeptide spacer and the anionically charged dye molecule.	7	34–126	< 5.3	3.8	—	No info on γ_i	0.00
21	Qin <i>et al.</i> [61]	CNT	1.59	805	51.0	9.9	0.0327	Subcontinuum	0.00
22	Qin <i>et al.</i> [61]	CNT	1.52	805	59.0	11.0	0.0330	Subcontinuum	0.00
23	Qin <i>et al.</i> [61]	CNT	1.42	805	103.0	18.1	0.0334	Subcontinuum	0.00
24	Qin <i>et al.</i> [61]	CNT	1.10	805	580.0	79.6	0.0352	Subcontinuum	0.00
25	Qin <i>et al.</i> [61]	CNT	0.98	805	354.0	43.2	0.0360	Subcontinuum	0.00
26	Qin <i>et al.</i> [61]	CNT	0.87	805	662.0	71.9	0.0369	Subcontinuum	0.00
27	Qin <i>et al.</i> [61]	CNT	0.81	805	882.0	89.2	0.0375	Subcontinuum	0.00
28	Sinha <i>et al.</i> [62]	CNT	250.00	10	1.0	0.0	0.0119	Subcontinuum 2.3	0.44

Continued.

TABLE I. Continued. Experimental data from the literature on water flow in nanomembranes versus our predictions. Here, for the calculation of $\Omega = (\rho\gamma/s/\mu^2)(s/d)^{0.2}$, the following parameters are assigned: $\rho = 997 \text{ kg/m}^3$, $s = 0.5 \text{ nm}$, $\mu = 1.002 \text{ mPa s}$, $\gamma_{i(\text{CNT-gr})\text{graphene}} = 83 \text{ mJ/m}^2$ [34], $\gamma_{i(\text{BNNT})} = 23 \text{ mJ/m}^2$ [56], $\gamma_{i(\text{polysulfone UF})} = 48.93 \text{ mJ/m}^2$ [57], and $\gamma_{i(\text{polycarbonate})} = 38.0 \text{ mJ/m}^2$ [58]. The values are selected based on the review summary provided in Table II.

No.	Ref.	Material	d (nm)	CNT length,		ϵ , Experiment	Slip length,		$\epsilon_{\text{our model}}$	$\mathcal{R}_p/\mathcal{R}_c$
				L (μm)	L (nm)		λ (nm)	Ω		
29	Du <i>et al.</i> [15]	MWCNT	10	4000		3403.0	4252.5	1529.9	2.22	0.01
30	Baek <i>et al.</i> [13]	CNT	4.8 ± 0.9	200		69039 ± 8122	41422.8 ± 4873	730 782.1	0.09	0.98
31	Baek <i>et al.</i> [13]	Ultrafiltration (UF) membrane	5.7 ± 2.5	0.1		5.8 ± 0.4	3.4 ± 0.3	4.7	1.24	0.19
32	Kim <i>et al.</i> [63]	CNT	3.3 ± 0.7	20–50		330.0	135.7	Subcontinuum	–	0.02
33	Lee <i>et al.</i> [16]	Flow in voids between CNTs - Outer-wall membrane	37.80	1300		203.9	958.9	11.4	17.92	0.00
34	Lee <i>et al.</i> [16]	Flow in voids between CNTs - Outer-wall membrane	28.80	1300		533.7	1917.8	23.0	23.17	0.01
35	Lee <i>et al.</i> [16]	Flow in voids between CNTs - Outer-wall membrane	15.80	1300		2047.1	4041.1	148.6	13.78	0.01
36	Lee <i>et al.</i> [16]	Flow in voids between CNTs - Outer-wall membrane	6.70	1300		14 885.5	12 465.8	27 846.8	0.53	0.05
37	Lee <i>et al.</i> [16]	Flow in voids between CNTs Thermally treated CNT - Outer-wall membrane	6.50	1300		36 247.2	29 450.0	39 496.1	0.92	0.11
38	Lee <i>et al.</i> [16]	CNT open ended (inner flow)	6.40	200		89 126.0	71 300.0	47 195.4	1.89	1.68
39	Zhang <i>et al.</i> [17]	CNT	10	120		210 000.0	262 498.8	1529.9	137.27	10.31
40	Bui <i>et al.</i> [64]	CNT	3.30	23 000		206.5 ± 119.5	84.8 ± 49.3	Subcontinuum	–	0.00
41	Yu <i>et al.</i> [65]	CNT	3	750		99 210.0	37 203.4	Subcontinuum	–	0.23
42	McGinnis <i>et al.</i> [66]	CNT	$0.67\text{--}1.27$	$0.5\text{--}1.5$		1000	83–158	Subcontinuum	–	0.57

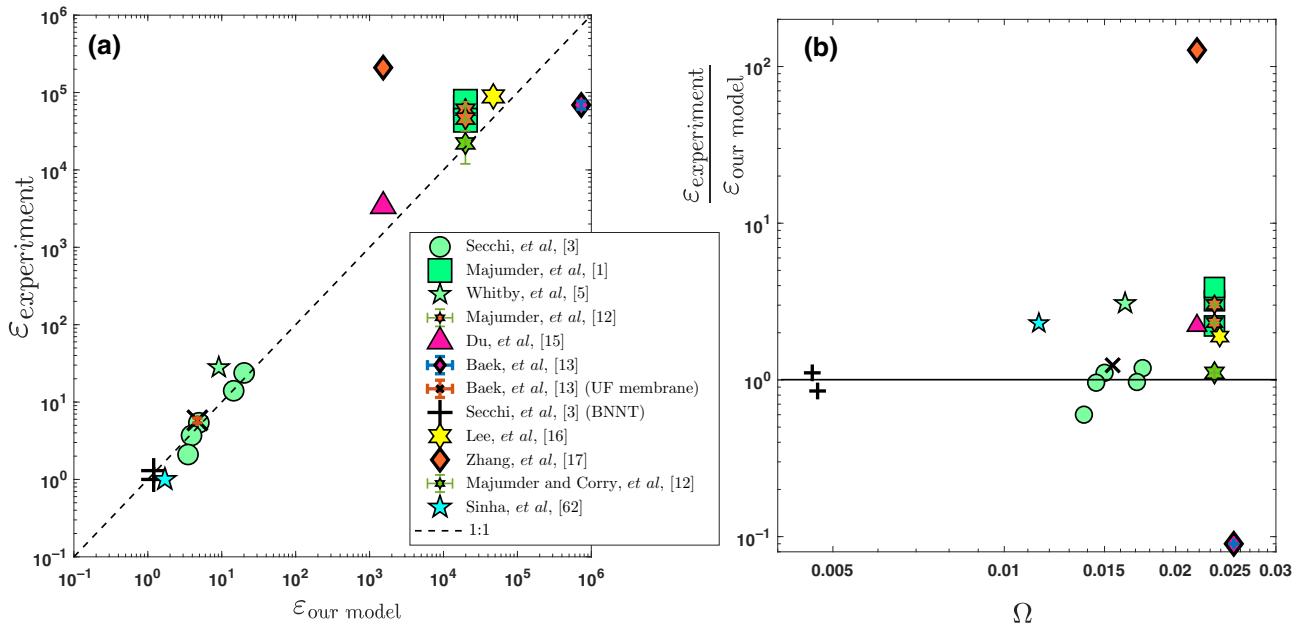


FIG. 5. Model predictions versus experimental data. (a) The model predictions of flow-rate-enhancement ratios, ε are shown versus the experimental values for continuum-flow experiments in CNTs (20 experiments). Untypical experiments and those affected by subcontinuum flow ($d \lesssim 3$ nm) are excluded. (b) The ratio between experimental measurements of ε and corresponding predictions of our model is shown versus the *slip-flow number*, Ω . This ratio approaches unity for the majority of data. The experiment conducted by Zhang *et al.* [17] that most deviates from our predictions can be highly affected by entrance effects with $\mathcal{R}_p/\mathcal{R}_c = 10.31$.

($L/\lambda > 1$) in which the entrance effects are negligible. When comparing experimental data from the literature to our model, we show if the entrance effects are significant or negligible (Table I). In most cases, the entrance effects are shown to be negligible. In a few cases, the entrance resistance can be effective on the flow rates for some factors up to at most a factor of 10. However, in those experiments, enhancement factors have been several orders of

magnitude suggesting that the model predictions based on channel flow could yet be practically reasonable, compared to the entrance effects, which are effective for only some factors.

In particular, Sisan and Lichter [68] showed that the experiments reported by Majumder *et al.* [1] can be up to 9 times faster than physically allowed values for frictionless tubes as they should be dominated by entrance

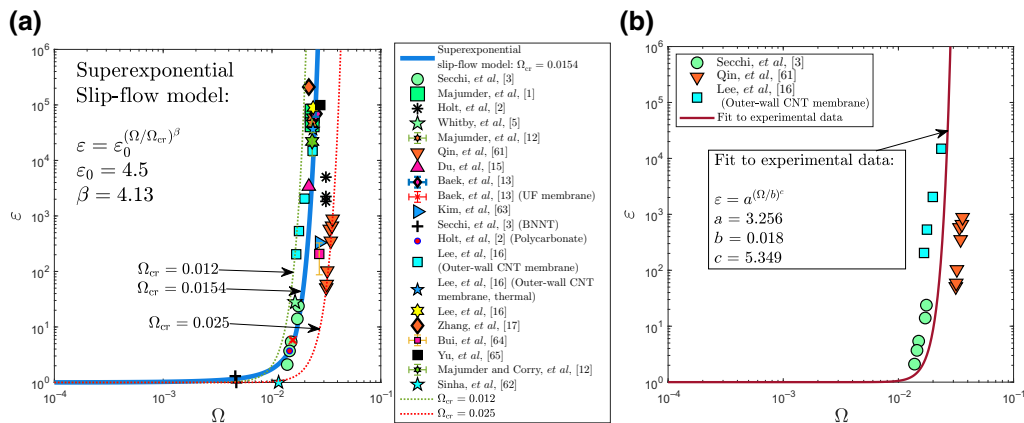


FIG. 6. Independent experimental derivation of model parameters (Ω_{cr} and β). (a) The analysis of experimental data suggests the range of $0.012 < \Omega_{cr} < 0.025$ by which the proposed superexponential model predicts %95 of the experimental data from 41 experiments. The computationally calculated value of $\Omega_{cr} = 0.0154$ lies within this range. (b) An equation is fitted ($\varepsilon = a(\Omega/b)^c$) to data from selected experiments in which all test conditions except the tube diameters have been constant. The analysis suggests a superexponential growth factor $c = 5.349$, close to the computationally derived value of $\beta = 4.13$ (in $\varepsilon = \varepsilon_0(\Omega/\Omega_{cr})^\beta$).

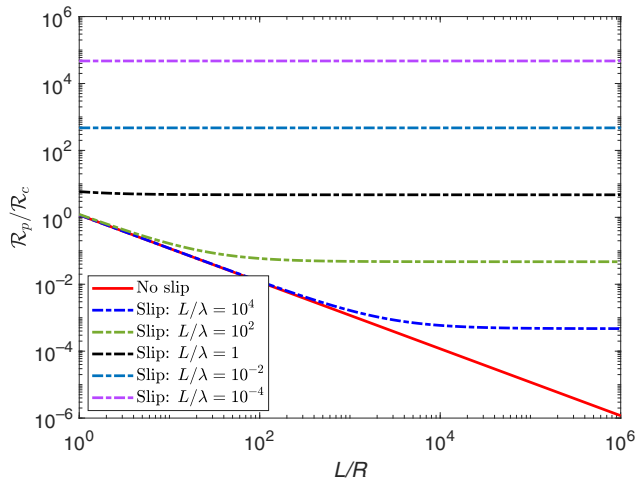


FIG. 7. Criteria for the significance of entrance effects. The ratio between the pore (entrance) hydrodynamic resistance and channel (tube) resistance, $\mathcal{R}_p/\mathcal{R}_c$ versus L/R where L and R are the channel length and radius, respectively. The viscous entrance effects are dominant when $\lambda > L$.

effects. We also show that $\mathcal{R}_p/\mathcal{R}_c$ for those experiments could be between 1.44 and 9.34 (Table I). The findings of Ref. [68] are also consistent with our work as the flow rates reported by Mjumder *et al.* are 2.21–3.8 times faster than our model predictions. Also the experiment reported by Zhang *et al.* [17] that most deviates from our predictions [Fig. 5(b)] should be highly affected by entrance effects with $\mathcal{R}_p/\mathcal{R}_c = 10.31$.

B. Continuum nanofluidic slip flow as iso- γ_i model behavior

In Fig. 8 we show our slip-flow model (shown as γ_i^{eff} contours) versus original data from experiments [Fig. 8(a)] and MD simulations [Fig. 8(b)] [62–66,69–75]. The original data are reported values of ε versus reported tube diameters, d . Thus the data points on Fig. 8 are pure literature data (with no assumptions) shown against the solution of our model (iso- γ_i^{eff} lines). The model can predict almost the whole range of experimental ε variations for CNTs in continuum regime ($d > 3$ nm) over 6 orders of magnitude [Fig. 8(a)] with finite variations of interface energies around the value of graphene ($\gamma_{i(\text{graphene})} = 83 \pm 7$ mJ/m² [34]). The flow mainly dominated by subcontinuum regime ($d < 3$ nm) appears to behave differently as the experimental data deviate from our model's iso- γ_i^{eff} contours at graphene's range.

In particular, Secchi *et al.* [3] and Lee *et al.* [7] have reported multiple experiments with constant test conditions except tube diameters (thus constant interfacial energies). These data lie within similar iso- γ_i^{eff} lines predicted

by our model in Fig. 8(a) further evidencing the validity of predictions.

Of particular relevance could be the similar iso- γ_i lines attributed to the data of Secchi *et al.* [3] (one of the most accurate measurements to date) and most of the other continuum-flow experiments as shown in Fig. 8(a). Similar γ_i levels indicating equivalent behaviors again suggest the feasibility of large ε in nanotubes with larger diameters, supporting many experiments [5,13,16,17].

C. functionalization effects

The role of energy levels can also describe the major impacts of functionalizations on flow enhancements [24,76]. For instance, chemical hydrophilic functionalization of 7-nm CNT membranes is reported by Majumder *et al.* to reduce ε for more than 4 orders of magnitude [14]. According to our model, a reduced γ_i from approximately equal to 83 [orange hexagrams in Fig. 8(a)], to approximately equal to 70 mJ/m² (black hexagram) and approximately equal to 50 mJ/m² (red hexagram) corresponds to original, tip, and core-functionalized nanotubes in this report, respectively.

D. Differences between CNTs and BNNTs

Insight into the surprising dissimilarity of CNTs and BNNTs (Secchi *et al.* [3]) could also be provided considering $\gamma_{i\text{BNNT}} = 21\text{--}26$ mJ/m² [56] being lower than $\gamma_{i\text{CNT}} = 83$ mJ/m² [34]. Such differences in γ_i match closely with the predictions of our model [see Fig. 8(a)]. This rationale can complete the *ab initio* findings [23] that linked the larger friction on boron nitride compared to graphene to a greater corrugation of free energy [23], but suggested only a threefold friction difference between CNTs and BNNTs, which was much smaller than experimental observations. Indeed, experiments revealed the differences between CNTs and BNNTs [3] in much greater scales where CNTs enhanced flow up to a factor of 100, but similarly sized BNNTs produced no flow enhancements. These differences convinced the authors of Ref. [3] to consider the corrugation effects as minor mechanisms and suggest mechanisms beyond these effects to describe the phenomenon. Now our findings here may further explain the actual scales of the differences between CNTs and BNNTs by potential differences of their interfacial energies.

E. The gap between experimental data and MD simulations

The proposed model sheds light on the significant gap between MD predictions and experimental data [large ε values reported in experiments for $d > 5$ nm, i.e., data in the highlighted ellipse in Fig. 8(a)]. The insufficiency of

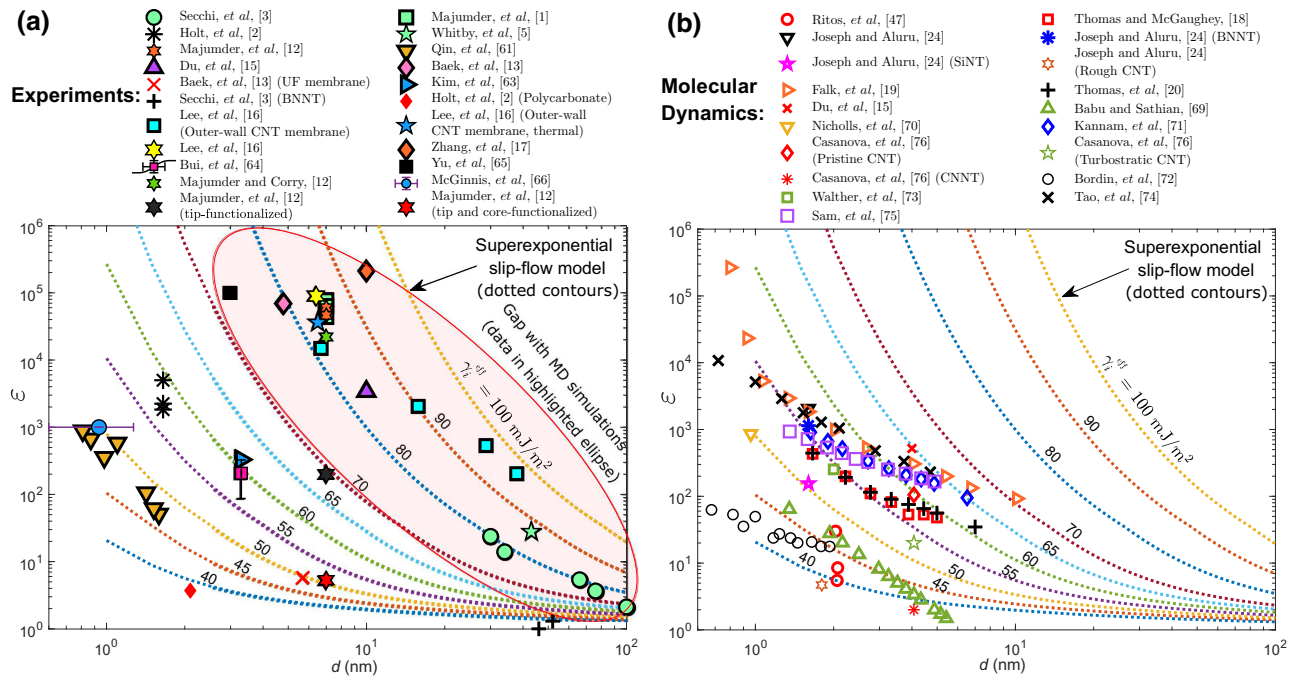


FIG. 8. Literature data for nanotube-water systems versus the universal (superexponential) slip-flow model. Original data as (d, ε) values from 42 experiments (a) and 97 MD simulations (b) are shown (see Appendix C for the details of MD data). Literature data points are for CNTs, unless mentioned otherwise. Our model is presented as dotted iso- γ_i^{eff} lines in both (a) and (b) as the solution of Eq. (4) i.e., $\varepsilon = f(\Omega) = f(d, \gamma_i, \text{constants})$ in which for Ω [Eq. (3)], the following parameters are assumed as constants: $\rho = 997 \text{ kg/m}^3$, $s = 0.5 \text{ nm}$, and $\mu = 1.002 \text{ mPa s}$. A large portion of experimentally reported (d, ε) values (data in the highlighted ellipse in (a)) have never been replicated by MD simulations (b). The cause of this significant gap is discussed in the text. Despite 6-orders-of-magnitude variations, the majority of experimental data in the continuum-slip regime ($d > 3 \text{ nm}$) shown in (a) can be explained well with our iso- γ_i^{eff} model with graphene’s value of $\gamma_i = 83 \pm 7 \text{ mJ/m}^2$ [34]. Subcontinuum experimental data ($d < 3 \text{ nm}$) appear to behave differently.

MD empirical force models to retrieve all hydrophobicity features including beyond vdW effects and hydrogen-bonding networks might be the reason for such a gap. Furthermore, when attempting to recover the interfacial (e.g., carbon-water) interactions in nanotubes, MD investigators have normally relied on the tuning of contact angles [77]. However, reproduction of the solid-liquid energy states as reference values rather than θ could be crucial in characterizing nonbounded interactions of water on graphene (see Ref. [32] for a detailed study). Thus, slight inaccuracies in intermolecular energy parameters used in MD simulations could also be the origin of significant deviations from experiments.

F. $\varepsilon - \theta$ relationship

Our model accounts for a combined role of contact angles, θ and surface energy, γ_s in flow-enhancement behaviors, as shown in Fig. 9. The graph illustrates how the flow slippage (enhancement) does not solely depend on θ ; hence even traditionally defined hydrophilic surfaces (with $\theta < 90^\circ$) can cause flow slippage depending on γ_s . Here the difference between a conventional definition of hydrophobicity ($\theta > 90^\circ$) and the principle of positive

interfacial energies used here is highlighted. Thus the findings can also explain the “unexpected” slip on surfaces with $\theta < 90^\circ$ observed in experiments [78,79] and simulations [49].

VII. CONCLUSION

A continuum approach coupled with interfacial force models in simulating solid-fluid intermolecular effects enabled us to provide an inclusive picture of continuum slip-flow regimes in nanofluidics. We show that the interfacial energies that originate the interfacial fluid viscosity and density variations can be responsible for ultrafast flows in nanotubes. The slip mechanism attributes to the variations of nanotube diameters and interfacial energies. We develop a universal model that quantifies flow-enhancement ratios of nanotubes and nanochannels as a superexponential function of a single dimensionless slip-flow number, Ω . The model could explain all previously measured flow enhancements filling a significant gap between experimental data and MD results. The model features a critical threshold (Ω_{cr}) beyond which the flow-enhancement ratios (ε) turn from a normal exponential to a superexponential growth. Insights are provided into

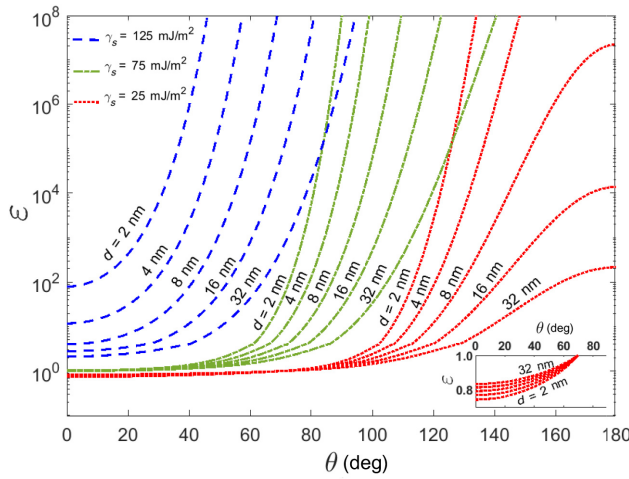


FIG. 9. Flow-enhancement ratio versus contact angle. The predicted ε depends on the tube diameter d , surface energy γ_s , and contact angles θ [via Young's Eq. (1)]. The inset magnifies the hydrophilic portion ($\varepsilon < 1$). Dependence of the flow enhancement on the energy state—instead of a sole contact angle—explains how moderately hydrophobic CNTs (with reported $\theta_{\text{graphene}} \approx 70^\circ\text{--}90^\circ$ [34–36], and $\theta_{\text{CNT}} \approx 70^\circ$ [37]) could induce extraordinary flow enhancements. The model differs from the few existing theoretical models that attribute typical flow enhancements observed in nanotubes to very large contact angles ($\theta > 150^\circ$) [29]. In calculating ε [Eq. (4)] as the function of Ω [Eq. (3)], the following parameters are assumed as constants: $\rho = 997 \text{ kg/m}^3$, $s = 0.5 \text{ nm}$, and $\mu = 1.002 \text{ mPa s}$.

long-standing puzzling observations in nanofluidic systems such as scattering of reported ε data by 6 orders of magnitude, 4-orders-of-magnitude decrease of ε due to hydrophilic functionalizations [14], and slippage of water on low-contact-angle surfaces [49,78]. We highlight a significant gap between previous MD simulations and experimental results where the ultrafast flow rates observed in wider than 5-nm tubes have never been computationally predicted by MD simulations (3-orders-of-magnitude differences in ε). Our study suggests the role of actual interfacial energy levels as a clue to addressing such a gap.

We limit our model to relatively long nanotubes (when entrance effects are negligible) in continuum-flow regimes ($d > 3 \text{ nm}$). The entrance effects are only significant when the slip lengths exceed the channel length. An analysis of the experimental data shows that the model predictions can be reasonably accurate for the majority of previous experiments.

Our model can reduce the complicated problem of functionalization effects on nanoscale permeability to a fundamental or experimental determination of the altered interfacial energy. This advancement could aid tailoring of separation membranes in which both permeability and selectivity of nanotubes are tunable [14,80] by reversible functionalization techniques [81,82], promising

broad applications in water purification, ion-exchange, and energy conversion.

ACKNOWLEDGMENTS

This research is funded by the Australian Research Council via the Discovery Projects (No. DPI120102188 and No. DP140100490). The authors also acknowledge support from the National Natural Science Foundation of China (Grant No. 51421006). The authors thank Professor Billy Todd for useful discussions.

APPENDIX A: COMPUTATIONAL DETAILS

1. Continuum-based simulation in nanofluidics

Despite the discrete nature of molecules in nanofluidic systems, a continuum-based approach has proved valid in describing the transport phenomena at the nanoscale [10,29,39]. The molecular dynamics and continuum hydrodynamics are shown to be different only in scales of a few layers of molecules [83–85]. As suggested by MD studies, for water nanofluidic systems, the limit of continuum transport mechanism (where the flow can be modeled using continuum-based relations) can be up to a channel width of about ten molecular diameters, i.e., $d > 3 \text{ nm}$ [59,60]. The characteristic length (tube diameter) of 1.66 nm is also proposed below which the transition to the subcontinuum mechanism takes place [10,18,29]. Thus, the majority of experiments of nanotube-flow systems can be studied using a continuum approach, provided that the interfacial features are properly captured. Lattice-Boltzmann is shown valid to investigate the nanoscale local hydrodynamic interactions, for example, in modeling lipid systems (with a grid spacing of approximately equal to 3 Å being sufficiently accurate) [86–88]. In our continuum framework, we adopt a lattice-Boltzmann approach with intermolecular potential for interfaces to account for the interfacial interactions averaged on the scales of the interface.

2. Lattice-Boltzmann method (LBM) with intermolecular potentials at interfaces

The Boltzmann equation reads

$$\frac{\partial f}{\partial t} + \mathbf{e} \cdot \nabla f + \mathbf{F} \cdot \nabla_{\mathbf{e}} f = \Omega_{\text{coll}}, \quad (\text{A1})$$

where the collision term $\Omega_{\text{coll}} = (f^{\text{eq}} - f)/\tau$ is the Bhatnagar-Gross-Krook (BGK) model, $f \equiv f(\mathbf{x}, \mathbf{e}, t)$ is the particle distribution function in the phase space (\mathbf{x}, \mathbf{e}) with t being the time, \mathbf{e} is the local molecular velocity, \mathbf{F} is the external force experienced by each fluid particle, f^{eq} is an equilibrium distribution function, and τ is the characteristic relaxation time.

The Navier-Stokes equations are shown to be recovered with the equilibrium distribution function given by [89]

$$f_i^{\text{eq}} = \omega_i \rho \left(1 + \frac{3(\mathbf{e}_i \cdot \mathbf{u})}{C^2} + \frac{9(\mathbf{e}_i \cdot \mathbf{u})^2}{2C^4} - \frac{3\mathbf{u}^2}{2C^2} \right), \quad (\text{A2})$$

where $C = \delta_x / \delta_t$ is the characteristic lattice velocity with δ_x being the time step and δ_x , the grid spacing. The weight factor ω_i is also assigned for each direction, the sum of which would be unity (see Ref. [90] for weight factors of different schemes). The study is performed using a D3Q19 scheme, while the parametric analyses on numerical variables (e.g., relaxation time) ensured the generality of the results [42].

The interparticle potential can be incorporated into the lattice-Boltzmann equation using a mean-field approximation [91]. Considering f^{eq} being the leading part of the distribution f , with the assumption of $\nabla_e f^{\text{eq}} \approx \nabla_e f$, the Boltzmann equation can be discretized in time and integrated leading to the following implicit expression [92]:

$$\begin{aligned} & f_i(\mathbf{x} + \mathbf{e}_i \delta_t, t + \delta_t) - f_i(\mathbf{x}, t) \\ &= \Omega_{\text{coll}} + \frac{\delta_t}{2} \left[f_i^F(\mathbf{x} + \mathbf{e}_i \delta_t, t + \delta_t) + f_i^F(\mathbf{x}, t) \right], \quad (\text{A3}) \end{aligned}$$

where f_i^F is the forcing term defined as [93]

$$f_i^F = \frac{\mathbf{F} \cdot (\mathbf{e}_i - \mathbf{u})}{\rho C^2} f_i^{\text{eq}}. \quad (\text{A4})$$

With a transformation defined as $\tilde{f}_i = f_i - (\delta t/2)f_i^F$ applied to Eq. (A3), we obtain an explicit solution for the Boltzmann equation incorporated with interparticle forces

$$\tilde{f}_i(\mathbf{x} + \mathbf{e}_i \delta t, t + \delta t) - \tilde{f}_i(\mathbf{x}, t) = \tilde{\Omega}_{\text{coll}} + \delta t f_i^F, \quad (\text{A5})$$

where $\tilde{\Omega}_{\text{coll}} = [\tilde{f}_i^{\text{eq}}(\mathbf{x}, t) - \tilde{f}_i(\mathbf{x}, t)/\tau]$ and $\tilde{f}_i^{\text{eq}} = \{1 - [\mathbf{F} \cdot (\mathbf{e}_i - \mathbf{u})/2\rho C^2]\delta t\} f_i^{\text{eq}}$.

The method implements a mean-field interparticle potential that can provide a semimesoscopic solution to the interfacial effects. Such molecular interactions that appear as interfacial energies averaged in scales of several molecular layers are treated in this method using solid-fluid attractive or repulsive forces (with different force models examined). The values of interfacial energies are calculated using the integration of the difference in the normal and transverse pressure tensor components obtained in lattice-Boltzmann (LB) simulations assuring the accuracy of the method for the level of fluid confinements.

3. Calculation of the interfacial energy in LBM simulations

The pressure tensor $\vec{\mathbf{P}}$ defined by $\vec{\nabla} \cdot \vec{\mathbf{P}} = \vec{\nabla}(c_s^2 \rho) - \vec{\mathbf{F}}$ where $\vec{\mathbf{F}}$ is the local boundary (interfacial) force acting on

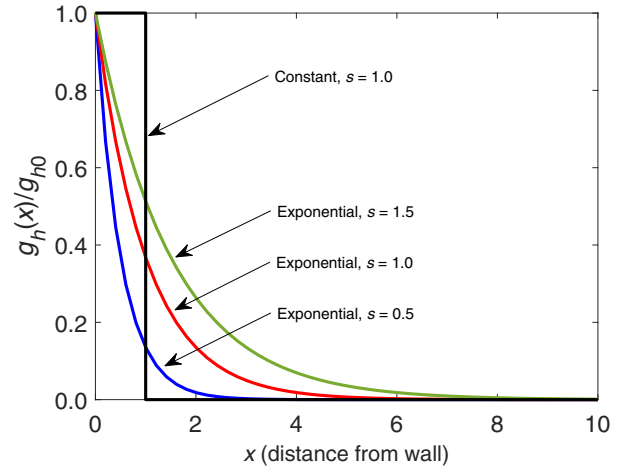


FIG. 10. Intermolecular solid-fluid force models implemented in this study, i.e., constant [$\mathbf{F}_h(x) = -\rho(x)\mathbf{g}_{h0}$ for $0 < x < s$ and $\mathbf{F}_h(x) = 0$ for $s < x$] and exponential decay [$\mathbf{F}_h(x) = -\rho(x)\mathbf{g}_h(x)$, where $\mathbf{g}_h(x) = \mathbf{g}_{h0}e^{-x/s}$].

the fluid (when setting $\Delta t = 1$) is equal to [94,95]

$$\begin{aligned} \vec{\mathbf{P}}_{\alpha\beta} = & \left(c_s^2 \rho + \frac{c_s^2 g_h}{2} \psi^2 + \frac{c_s^4 g_h}{4} (\vec{\nabla} \psi)^2 + \frac{c_s^4 g_h}{2} \psi \Delta \psi \right) \delta_{\alpha\beta} \\ & - \frac{c_s^4 g_h}{2} (\partial_\alpha \psi)(\partial_\beta \psi). \quad (\text{A6}) \end{aligned}$$

The variable g_h specifies the intensity of the boundary (interfacial) force. This force is implemented in this study as a constant, $g_h(x) = g_{h0}$ or an exponentially decaying function of x , $g_h(x) = g_{h0}e^{-x/s}$ with different values for s where x is the distance from boundaries (see Fig. 10). The pseudopotential ψ is given as $\psi(x) = \rho(x)$. We calculate the solid-fluid interfacial energy for an assumed planar interface at $x = 0$ using the pressure tensor in Eq. (A6) [94,95]

$$\gamma_i = \int_0^L (P_{xx} - P_{yy}) dx = -\frac{c_s^4}{2} \int_0^L g_h \left(\frac{d\psi}{dx} \right)^2 dx. \quad (\text{A7})$$

The length L is the length on which the boundary (interfacial) force is effective.

We calculate the solid-liquid interfacial energy with Eq. (A7) for each simulation (with a cellwise integration) where the boundary force is implemented. It is worth mentioning that the relation between the force coefficient g_h and the resulting interfacial energy is nonlinear as demonstrated in Fig. 11.

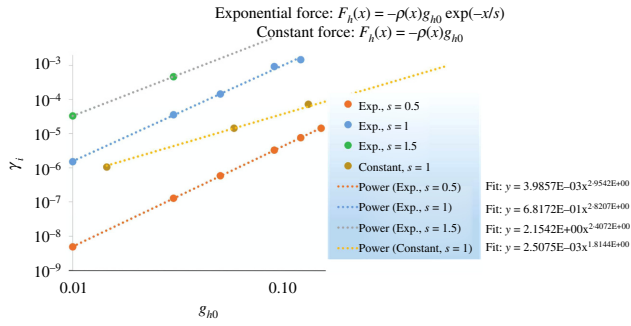


FIG. 11. Nonlinear relationship between the solid-fluid force intensity coefficient g_{h0} and the resulting interfacial energy γ_i (in lattice units) for different intermolecular solid-fluid force models (constant or exponentially decaying forces). For each force model (constant and exponentially decaying), we change the force factors (force intensity coefficient g_{h0} and the decay length s). γ_i is calculated through a cellwise integration of the pressure tensor as per Eq. (A7). The power functions are fitted to each set of simulation data with a specific force function and s .

4. Determination of the factor α in the definition of Ω

We define a dimensionless *slip-flow number* Ω as follows:

$$\Omega = \frac{\rho\gamma_i^{\text{eff}}d}{\mu^2} \left(\frac{s}{d}\right)^\alpha. \quad (\text{A8})$$

To determine the coefficient α in Eq. (A8), we implement a least-squares fitting analysis on the subcritical portion of the results (ε versus Ω) for all simulations including tubes (with different diameters) and parallel plates (with various spacing) and variable intensities of interfacial energies.

The data points can be fitted to a biexponential function up to the limit of the critical value of *slip-flow number*, Ω_{cr} beyond which the behavior of ε begins to deviate from any normal exponential function with a fast surge in the increase rate (see Fig. 12). We select α in such a way to make all data (curves) best collapse into a single curve. The unified model is achieved by minimizing the sum of square errors (differences), SSE, for all datasets (Fig. 13). The value of $\alpha = 1.2$ is found to produce the minimum SSE for the subcritical portion of the results, giving the best convergence of all curves to a unified behavior. The resulting Ω also provides a unified trend in critical regime where Ω exceeds the critical value, which suggests the universality of Ω with $\alpha=1.2$ in describing the nanofluidic slip-flow regimes.

5. Interfacial energy values for nanotube materials

Experimental reports on wetting properties of nanotube materials are reviewed in Table II.

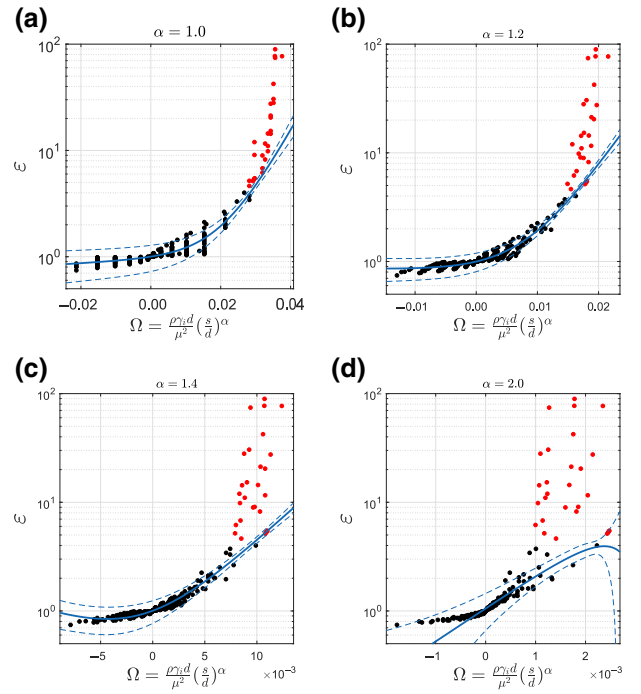


FIG. 12. Biexponential function fitted to the subcritical portion of the $\varepsilon - \Omega$ values with $\alpha = 1.0$ (a), 1.2 (b), 1.4 (c), and 2.0 (d) used in the definition of $\Omega = \frac{\rho\gamma_i d}{\mu^2} \left(\frac{s}{d}\right)^\alpha$. The red data points are those in the critical regime, which are excluded from the fitting. The fitted function appears in blue with the dashed lines indicating the prediction bounds with 95% confidence.

6. Biexponential and superexponential coefficients

In Fig. 14, we provide more details on the fitting coefficients of the subcritical and critical slip-flow regimes.

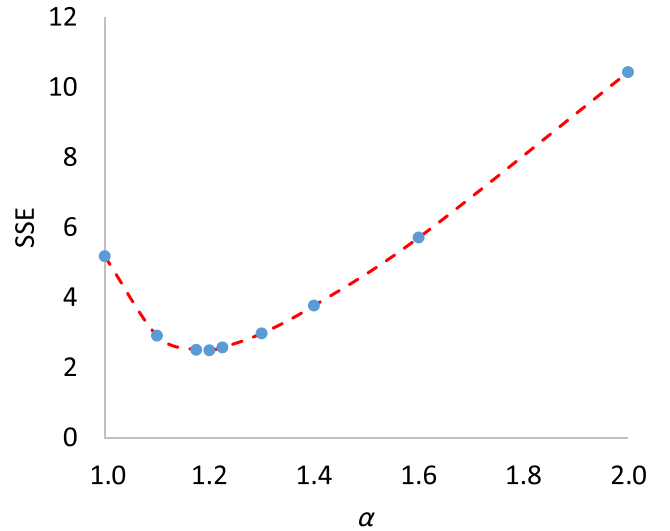


FIG. 13. Sum of square differences and errors versus α in $\Omega = \frac{\rho\gamma_i d}{\mu^2} \left(\frac{s}{d}\right)^\alpha$. The value of $\alpha = 1.2$ gives the minimum SSE (best collapses all curves into a unified model).

TABLE II. Wetting properties of nanotube materials reported in the literature. Values of the interfacial energies are either reported directly in references (values with no parentheses) or calculated using Young's equation based on the contact angle and the surface energy provided by each reference (values in parentheses).

Substance	Single Layer (SL) or Multi Layer (ML)	Method	Surface energy γ_s (mJ/m ²)	Substance-water interfacial energy γ_i (mJ/m ²)	Contact angle of water θ (degree)	Remarks	Ref.
Graphene	SL	Experimental	115 ± 4	(91.5 ± 3)	71 ± 1	Chemical vapor deposition (CVD)	[34]
Graphene	ML	Experimental	119 ± 3	83 ± 7	70 ± 1	Direct measurement of γ_i , CVD	[34]
Graphene	SL-ML	Experimental	46.7	(90.5)	127 ± 4	—	[45]
Graphene	ML	Experimental	—	—	90.6 – 94.2	—	[35]
Graphene	SL-ML	Experimental	—	—	93	Independent of number of layers and substrate (Copper, SiO ₂ , Glass, HOPG)	[96]
Graphene	—	Molecular dynamics	—	99.1 ^a , 93.8 ^b	—	^a Ewald sum method, ^b Reaction field method	[46]
Graphene	SL-ML	Experimental	—	—	92	Graphene on SiC substrate	[97]
CNT	ML	Experimental	45.3	—	—	—	[98]
CNT	Pristine ML	Experimental	42.2	—	—	—	[99]
Individual BNNT	—	Experimental	26.7	21.1–25.8	85.4 ± 4.9	Wilhelmy method	[56]
BN powder	—	Experimental	43.8 ^a , 66 ^b	(19.2 ^a , 5.6 ^b)	70 ^a , 33 ^b	^{a,b} Two different samples	[100]
Polycarbonate	—	Experimental	38	(38)	90	175 – μ m-thick films	[58]
Polycarbonate	—	Experimental	42.5 ^a , 66 ^b	(16.7 ^a , –0.6 ^b)	69 ^a , 22.3 ^b	^a 1 and ^b 120-min UV treatment	[101]
Polysulfone	—	Experimental	45.57 ± 4.45	(48.93 ± 4.5)	92.65	Rame-Hart contact angle goniometer	[57]
Polysulfone	—	Experimental	39 ^a , 65 ^b	(10.9 ^a , 4.6 ^b)	67 ^a , 33 ^b	Ultrafiltration (UF) membrane ^a 1 and ^b 120-s oxygen plasma treatment	[102]
Polysulfone	—	Experimental	42.56	(22.71)	74	—	[103]

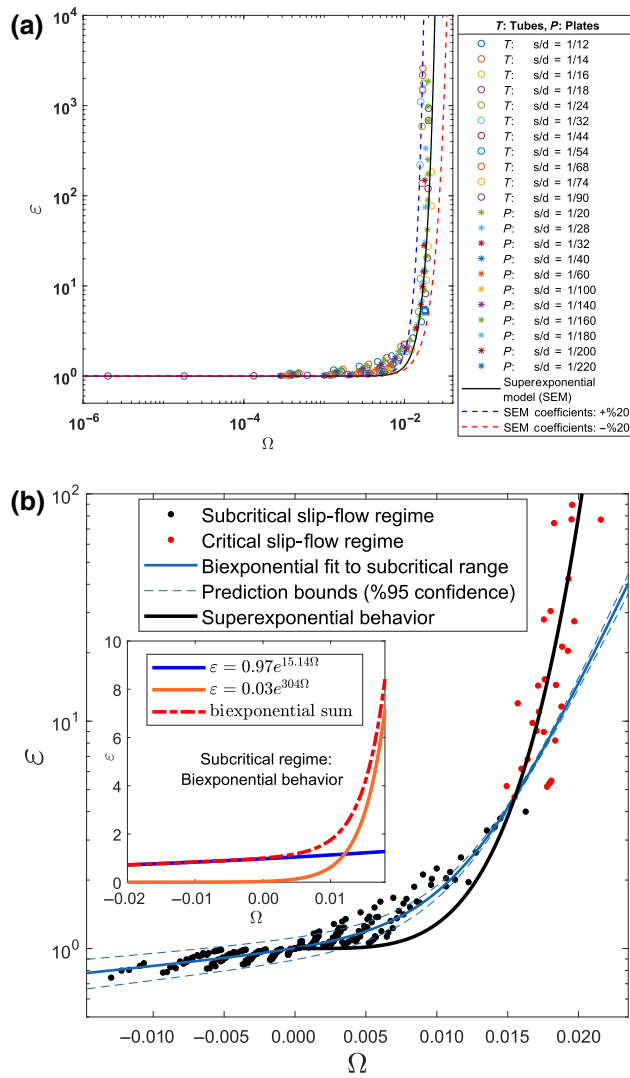


FIG. 14. (a) Variation of the superexponential model coefficients. The optimized coefficients, i.e., $(\varepsilon_0, \Omega_{cr}, \beta)$ are multiplied by $(1.2, 0.8, 1.2)$ and $(0.8, 1.2, 0.8)$ to determine a $+20\%$ and -20% variation of coefficients, respectively. (b) The superexponential slip-flow model shown together with the biexponential behavior of slip flow in the subcritical regime. While the subcritical behavior is best characterized by the biexponential fit, with Ω exceeding the critical value ($\Omega_{cr} \approx 0.0154$), a superexponential fit would be the best representative of the ultrafast slip-flow behavior. The inset illustrates the sum of exponential terms in the biexponential model for the subcritical regime where the first term ($\varepsilon = 0.97e^{15.14\Omega}$) best represents the flow attenuation behavior (hydrophilic effects). The biexponential sum of both terms ($\varepsilon = 0.97e^{15.14\Omega} + 0.03e^{30.4\Omega}$) can properly fit the moderate flow-enhancement behavior (due to hydrophobic effects) in the subcritical regime.

7. Universality of the slip-flow model ($\Omega - \varepsilon$ behavior)

Our model is proposed as a function of the nondimensional *slip-flow number* Ω . To demonstrate the universality of this function, we conduct a large number of simulations

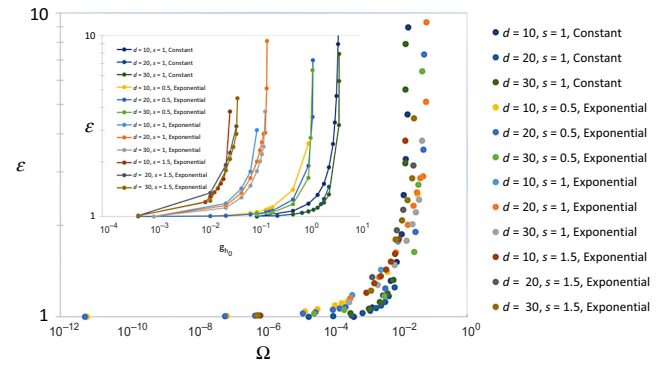


FIG. 15. Universality of the proposed slip-flow model as a function of the *slip-flow number* Ω . Here ε versus Ω is shown for the different force models used (constant or exponentially decaying with various decay lengths, s), all collapsing into a unified behavior as given by the superexponential model. The proposed *slip-flow number* Ω is demonstrated to be a physically meaningful number in unifying the slip-flow regime independent of the force models and their lengths of influence. The inset illustrates the same simulation data but shown as ε versus g_{h0} —in lattice units—(where the constant force model is $\mathbf{F}_h(x) = -\rho(x)\mathbf{g}_{h0}$, $0 < x < s$ and the exponential model is $\mathbf{F}_h(x) = -\rho(x)\mathbf{g}_{h0}e^{-x/s}$ with x being the distance from walls). The inset shows the broad scatter of the slip-flow behaviors in contrast with the single behavior obtained using the *slip-flow number*.

for flow in tubes and between parallel plates with variable diameters and separation spaces. We also simulate a variety of cases, from repulsive to attractive solid-fluid forces, with different levels of interfacial energies. It is shown in Fig. 2 of the main paper that all cases can be unified into a single behavior with our dimensionless *slip-flow number*, Ω .

To further evaluate the universality of our model, we also implemented different force models (constant and exponentially decaying: see Fig. 10). In addition, we change the decay length of the exponentially decaying forces (s). The proposed *slip-flow number* Ω is shown to universally characterize the slip-flow regimes with a unique behavior for all cases under a wide range of conditions, as illustrated in Fig. 15.

APPENDIX B: DISCUSSIONS ON THE VARIATION OF MODEL PARAMETERS IN NANOTUBE-WATER SYSTEMS

1. Variation of viscosity, μ

Indicated by many experiments [104,105] and MD simulations [18,106], the viscosity of confined water varies spatially within an interface region near the walls where it is significantly affected by interfacial interaction. The interfacial region is determined as the water layer with a critical thickness next to the wall surface. The viscosity retains the value of bulk fluid for interior water beyond the

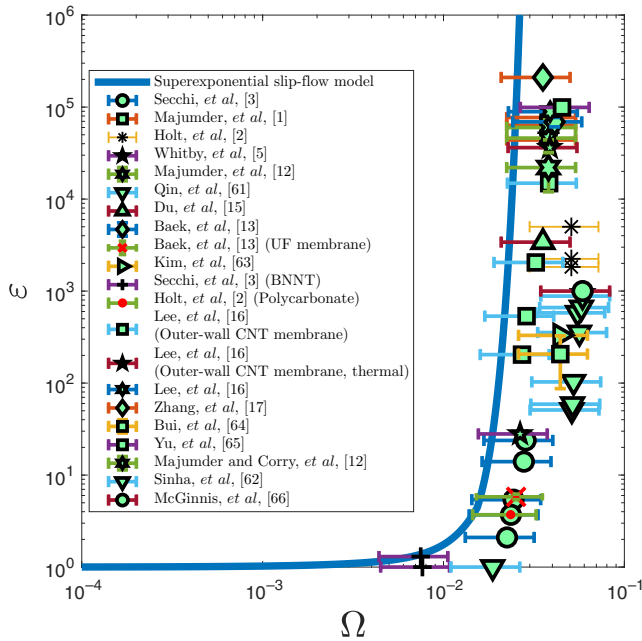


FIG. 16. Supereponential model versus experimental data (as summarized in Table I) where data points correspond to the assumption of $s = 0.75$ nm and errorbars correspond to the variation of s in range of 0.5–1 nm.

critical thickness. The critical thickness of the interfacial region is investigated by several studies (reviewed in Ref. [29]), with a thickness of 0.7 nm suggested as an average [18,29].

Some researchers have suggested that the viscosity of water in the interface region could be a function of the contact angle [29]. Fitted to some datasets from mainly MD simulations, the following linear relationship is proposed for the ratio of the interfacial viscosity to the viscosity for the bulk fluid, μ_i/μ_∞ and the contact angle, θ (degree) [29]:

$$\frac{\mu_i}{\mu_\infty} = -0.018\theta + 3.25. \quad (\text{B1})$$

We argue that the use of a sole contact angle criterion based on MD simulations is inadequate for determining the interfacial characteristics of the nanofluidic systems. The interfacial energy states in addition to the contact angle—which is a tunable factor in MD simulations—could be a critical point to investigate the interface fluid properties in nanoscales [32]. In our model, the dynamic viscosity for the bulk fluid is used to calculate the *slip-flow number*, Ω while the subinterface variations are intrinsically accounted for by the value of the interfacial energy. As viscosity can be a nonlocal property of the highly confined fluid, care has been taken to ensure the transport coefficients are valid when selecting the simulation scales.

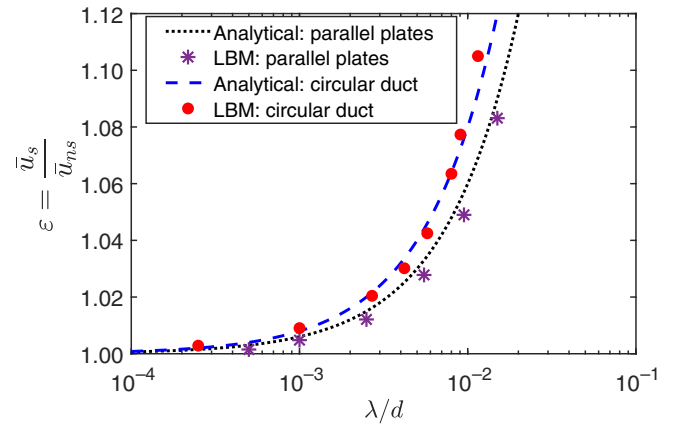


FIG. 17. Comparison of numerical results with analytical solutions for flow-enhancement ratios versus normalized slip lengths. The analytical solutions are $\epsilon = (1 + 6\lambda/d)$ for parallel plates (with separation distance of d) and $\epsilon = (1 + 8\lambda/d)$ for circular ducts (with diameter d) [118].

2. Variation of interfacial layer characteristic thickness, s

Although a conclusive law for hydrophobic interactions (between two hydrophobic surfaces in water) is yet to be achieved [107], an exponentially decaying behavior is usually observed in direct measurements [26,108,109]. There has also been a long-lasting debate on the range of hydrophobic interactions. However, direct measurements of hydrophobic forces between two surfaces in aqueous solutions using atomic force microscopy have revealed a pure hydrophobic interaction exponentially decaying over distances up to 10–20 nm with a decay length of 0.3–2 nm, averagely approximately 1 nm [27,28,107]. For the measurement of such pure hydrophobic forces, the surfaces are required to be smooth, continuous, free from defects, and stable in water. The long-range attractive forces measured in larger ranges from > 200 nm up to thousands of nm are also believed to be associated with surface-preparation techniques [27], and not the pure hydrophobicity. Overall, a typical value of approximately 1 nm is suggested as the decay length of both hydrophobic and hydrophilic interactions [28], i.e., the forces between two surfaces in water.

The characteristic length of 1 nm concluded for both hydrophobic and hydrophilic (solid-solid) interactions between two surfaces in water [28] could be assumed as an upper limit for s , which is the characteristic length of the solid-fluid effects (for a single surface in water). Those solid-fluid effects (which result in interfacial energies) are the origin of the solid-solid hydrophobic and hydrophilic interactions. In this study, considering the overlapping of hydrophobic effects, we assume a value of 0.5 nm as s (force characteristic length for a single solid surface in water), equivalent to half of the decay length of

TABLE III. MD simulation data from the literature on water flow in nanotubes.

No.	Ref.	Method	Material	d (nm)	ϵ	Slip length (nm)
1	Ritos <i>et al.</i> [47]	MD	CNT	2.03	30.00	7.37
2	Ritos <i>et al.</i> [47]	MD	BNNT	2.07	8.50	1.94
3	Ritos <i>et al.</i> [47]	MD	SiCNT	2.06	5.50	1.16
4	Thomas <i>et al.</i> [18]	MD	CNT	1.66	432.47	89.53
5	Thomas <i>et al.</i> [18]	MD	CNT	2.22	198.70	54.86
6	Thomas <i>et al.</i> [18]	MD	CNT	2.77	110.39	37.88
7	Thomas <i>et al.</i> [18]	MD	CNT	3.33	81.82	33.64
8	Thomas <i>et al.</i> [18]	MD	CNT	3.88	53.25	25.34
9	Thomas <i>et al.</i> [18]	MD	CNT	4.44	53.25	29.00
10	Thomas <i>et al.</i> [18]	MD	CNT	4.99	48.05	29.35
11	Joseph and Aluru [24]	MD	CNT	1.60	2052.00	410.20
12	Joseph and Aluru [24]	MD	BNNT	1.60	1142.00	228.20
13	Joseph and Aluru [24]	MD	Si NT	1.60	155.00	30.80
14	Joseph and Aluru [24]	MD	Rogh NT	1.80	4.70	0.83
15	Falk <i>et al.</i> [19]	MD	CNT	10.13	92.30	115.61
16	Falk <i>et al.</i> [19]	MD	CNT	6.75	133.14	111.49
17	Falk <i>et al.</i> [19]	MD	CNT	5.40	199.01	133.65
18	Falk <i>et al.</i> [19]	MD	CNT	4.05	306.22	154.52
19	Falk <i>et al.</i> [19]	MD	CNT	2.68	534.24	178.64
20	Falk <i>et al.</i> [19]	MD	CNT	2.02	981.48	247.57
21	Falk <i>et al.</i> [19]	MD	CNT	1.60	1845.59	368.92
22	Falk <i>et al.</i> [19]	MD	CNT	1.34	2944.73	493.08
23	Falk <i>et al.</i> [19]	MD	CNT	1.07	5298.85	708.59
24	Falk <i>et al.</i> [19]	MD	CNT	0.93	23 318.28	2710.63
25	Falk <i>et al.</i> [19]	MD	CNT	0.80	266 194.13	26 619.31
26	Thomas <i>et al.</i> [20]	MD	CNT	7.00	34.74	29.50
27	Thomas <i>et al.</i> [20]	MD	CNT	4.99	56.03	34.32
28	Thomas <i>et al.</i> [20]	MD	CNT	4.44	65.44	35.76
29	Thomas <i>et al.</i> [20]	MD	CNT	3.88	75.52	36.14
30	Thomas <i>et al.</i> [20]	MD	CNT	3.33	90.33	37.18
31	Thomas <i>et al.</i> [20]	MD	CNT	2.77	114.72	39.37
32	Thomas <i>et al.</i> [20]	MD	CNT	2.22	191.87	52.97
33	Thomas <i>et al.</i> [20]	MD	CNT	1.66	443.49	91.82
34	Du <i>et al.</i> [15]	MD	CNT	4.00	520.00	259.50
35	Babu <i>et al.</i> [69]	MD	CNT	5.42	1.49	0.33
36	Babu <i>et al.</i> [69]	MD	CNT	5.16	1.72	0.46
37	Babu <i>et al.</i> [69]	MD	CNT	4.88	2.00	0.61
38	Babu <i>et al.</i> [69]	MD	CNT	4.33	2.82	0.98
39	Babu <i>et al.</i> [69]	MD	CNT	4.07	3.37	1.20
40	Babu <i>et al.</i> [69]	MD	CNT	3.79	4.10	1.47
41	Babu <i>et al.</i> [69]	MD	CNT	3.52	5.05	1.79
42	Babu <i>et al.</i> [69]	MD	CNT	3.25	6.34	2.17
43	Babu <i>et al.</i> [69]	MD	CNT	2.98	8.17	2.67
44	Babu <i>et al.</i> [69]	MD	CNT	2.50	13.48	3.89
45	Babu <i>et al.</i> [69]	MD	CNT	2.16	20.21	5.19
46	Babu <i>et al.</i> [69]	MD	CNT	1.93	27.81	6.48
47	Babu <i>et al.</i> [69]	MD	CNT	1.35	64.24	10.68
48	Nicholls <i>et al.</i> [70]	MD	CNT	0.96	860.00	103.08
49	Kannam <i>et al.</i> [71]	MD	CNT	6.52	95.05	76.59
50	Kannam <i>et al.</i> [71]	MD	CNT	4.87	155.85	87.11
51	Kannam <i>et al.</i> [71]	MD	CNT	4.34	181.28	92.81
52	Kannam <i>et al.</i> [71]	MD	CNT	3.80	206.70	98.10
53	Kannam <i>et al.</i> [71]	MD	CNT	3.26	260.48	100.92
54	Kannam <i>et al.</i> [71]	MD	CNT	2.71	337.44	121.82
55	Kannam <i>et al.</i> [71]	MD	CNT	2.16	517.50	131.63
56	Kannam <i>et al.</i> [71]	MD	CNT	1.90	664.24	157.49

Continued.

TABLE III. MD simulation data from the literature on water flow in nanotubes.

No.	Ref.	Method	Material	d (nm)	ε	Slip length (nm)
57	Kannam <i>et al.</i> [71]	MD	CNT	1.63	911.49	174.72
58	Casanova <i>et al.</i> [76]	MD	Pristine CNT	4.07	105.15	53.00
59	Casanova <i>et al.</i> [76]	MD	Turbostratic CNT	4.07	20.07	9.70
60	Casanova <i>et al.</i> [76]	MD	Carbon-nitride nanotube	4.07	<2.97	<1
61	Bordin <i>et al.</i> [72]	MD	CNT	1.93	17.71	4.03
62	Bordin <i>et al.</i> [72]	MD	CNT	1.79	17.78	3.75
63	Bordin <i>et al.</i> [72]	MD	CNT	1.65	20.71	4.06
64	Bordin <i>et al.</i> [72]	MD	CNT	1.45	20.10	3.47
65	Bordin <i>et al.</i> [72]	MD	CNT	1.37	23.72	3.88
66	Bordin <i>et al.</i> [72]	MD	CNT	1.24	27.36	4.08
67	Bordin <i>et al.</i> [72]	MD	CNT	1.17	23.82	3.34
68	Bordin <i>et al.</i> [72]	MD	CNT	1.00	49.62	6.07
69	Bordin <i>et al.</i> [72]	MD	CNT	0.90	35.39	3.87
70	Bordin <i>et al.</i> [72]	MD	CNT	0.82	53.29	5.36
71	Bordin <i>et al.</i> [72]	MD	CNT	0.68	62.65	5.22
72	Bordin <i>et al.</i> [72]	MD	CNT	0.51	102.02	6.48
73	Bordin <i>et al.</i> [72]	MD	CNT	0.48	118.46	7.03
74	Bordin <i>et al.</i> [72]	MD	CNT	0.43	124.92	6.72
75	Bordin <i>et al.</i> [72]	MD	CNT	0.41	211.35	10.88
76	Bordin <i>et al.</i> [72]	MD	CNT	0.38	277.80	13.13
77	Walther <i>et al.</i> [73]	MD	CNT	2.00	253.00	63.00
78	Tao <i>et al.</i> [74]	MD	CNT	101.07	1.00	0.00
79	Tao <i>et al.</i> [74]	MD	CNT	4.71	230.00	134.76
80	Tao <i>et al.</i> [74]	MD	CNT	3.73	332.73	154.57
81	Tao <i>et al.</i> [74]	MD	CNT	2.89	481.54	173.57
82	Tao <i>et al.</i> [74]	MD	CNT	2.10	1046.83	274.76
83	Tao <i>et al.</i> [74]	MD	CNT	1.79	1285.87	287.89
84	Tao <i>et al.</i> [74]	MD	CNT	1.53	1783.96	340.71
85	Tao <i>et al.</i> [74]	MD	CNT	1.26	2912.73	459.67
86	Tao <i>et al.</i> [74]	MD	CNT	1.00	5161.59	645.07
87	Tao <i>et al.</i> [74]	MD	CNT	0.72	10776.59	969.38
88	Sam <i>et al.</i> [75]	MD	CNT (zigzag)	4.89	166.47	101.11
89	Sam <i>et al.</i> [75]	MD	CNT (zigzag)	4.34	185.60	100.15
90	Sam <i>et al.</i> [75]	MD	CNT (zigzag)	3.78	218.66	102.89
91	Sam <i>et al.</i> [75]	MD	CNT (zigzag)	3.23	251.73	101.34
92	Sam <i>et al.</i> [75]	MD	CNT (zigzag)	2.72	326.63	110.54
93	Sam <i>et al.</i> [75]	MD	CNT (zigzag)	2.43	362.67	109.92
94	Sam <i>et al.</i> [75]	MD	CNT (zigzag)	2.15	443.31	118.72
95	Sam <i>et al.</i> [75]	MD	CNT (zigzag)	1.88	537.90	126.39
96	Sam <i>et al.</i> [75]	MD	CNT (zigzag)	1.59	718.88	142.57
97	Sam <i>et al.</i> [75]	MD	CNT (zigzag)	1.36	933.35	157.96

hydrophobic and hydrophilic interactions (for two surfaces in water).

We also examine the validity of the model when considering the variations of the value of s , i.e., the interfacial layer characteristic thickness (the solid-fluid force characteristic length). For this purpose, we plot our model versus the experimental values obtained from the literature (as summarized in Table I), with a choice of s in the range of 0.5–1 nm (see Fig. 16). As evident from the figure, the model predictions lie close to the data (varied with the assumed range of s), where Ω_{cr} obtained from simulations is within the same order suggested by data variations.

3. Variation of density, ρ

The variation of density is dominant in sub-1.6-nm dimensions where the subcontinuum transport is evident [61,110,111], extended up to 2.4-nm diameters with the effects of first molecular layers [111,112]. Nevertheless, while the density can increase or decrease up to a few folds in the subcontinuum regime or in the interfacial layers, the effective density in larger diameters is different from the bulk only in few percentages. The effective density can lead to the bulk value in upper-2.4-nm diameter tubes [111,112]. Overall, the density variations are in much lower ranges than those of viscosity. Similar to

viscosity, a bulk value is used in calculation of Ω in our model and density variations in interfacial layers are intrinsically accounted for in calculating the interfacial energies.

APPENDIX C: MODEL VALIDATION

1. Slip-flow numerical model versus analytical solutions

The validity of the numerical method in capturing the slip-flow characteristics as induced by the fluid-solid wettability has been evaluated in previous studies [42,113–117] and also here against the analytical solution (Fig. 17). Under the influence of hydrophobic solid-fluid effects (forces resulting in interfacial energies), the velocity profiles deviate from those with a no-slip boundary-wall assumption. Deviated velocity profiles result in increased mean velocity and an apparent slip length (when extrapolating the velocity profiles). Here, we implement the solid-fluid repulsive (hydrophobic) forces. Then the mean flow velocity and the apparent slip lengths (from extrapolated profiles) are calculated. In Fig. 17, we show that the velocity enhancements and corresponding slip lengths due to deviated velocity profiles are in agreement with the analytical relations available for the pipe flow and the flow between plates.

2. Numerical (MD) literature data for nanotube-water flow systems

A summary of the parameters used to produce Fig. 8, extracted from molecular-dynamics simulations on nanotubes reported in the literature is given in Table III.

-
- [1] M. Majumder, N. Chopra, R. Andrews, and B. J. Hinds, Nanoscale hydrodynamics: Enhanced flow in carbon nanotubes, *Nature* **438**, 44 (2005).
 - [2] J. K. Holt, H. G. Park, Y. Wang, M. Stadermann, A. B. Artyukhin, C. P. Grigoropoulos, A. Noy, and O. Bakajin, Fast mass transport through sub-2-nanometer carbon nanotubes, *Science* **312**, 1034 (2006).
 - [3] E. Secchi, S. Marbach, A. Niguès, D. Stein, A. Siria, and L. Bocquet, Massive radius-dependent flow slippage in carbon nanotubes, *Nature* **537**, 210 (2016).
 - [4] H. Huang, Z. Song, N. Wei, L. Shi, Y. Mao, Y. Ying, L. Sun, Z. Xu, and X. Peng, Ultrafast viscous water flow through nanostrand-channelled graphene oxide membranes, *Nat. Commun.* **4**, 2979 (2013).
 - [5] M. Whitby, L. Cagnon, M. Thanou, and N. Quirke, Enhanced fluid flow through nanoscale carbon pipes, *Nano Lett.* **8**, 2632 (2008), PMID: 18680352.
 - [6] R. Das, M. E. Ali, S. B. A. Hamid, S. Ramakrishna, and Z. Z. Chowdhury, Carbon nanotube membranes for water purification: A bright future in water desalination, *Desalination* **336**, 97 (2014).

- [7] C. H. Lee, N. Johnson, J. Drelich, and Y. K. Yap, The performance of superhydrophobic and superoleophilic carbon nanotube meshes in water–oil filtration, *Carbon* **49**, 669 (2011).
- [8] A. Srivastava, O. Srivastava, S. Talapatra, R. Vajtai, and P. Ajayan, Carbon nanotube filters, *Nat. Mater.* **3**, 610 (2004).
- [9] A. Siria, P. Poncharal, A.-L. Biance, R. Fulcrand, X. Blase, S. T. Purcell, and L. Bocquet, Giant osmotic energy conversion measured in a single transmembrane boron nitride nanotube, *Nature* **494**, 455 (2013).
- [10] J. A. Thomas and A. J. McGaughey, Water Flow in Carbon Nanotubes: Transition to Subcontinuum Transport, *Phys. Rev. Lett.* **102**, 184502 (2009).
- [11] G. Hummer, J. C. Rasaiah, and J. P. Noworyta, Water conduction through the hydrophobic channel of a carbon nanotube, *Nature* **414**, 188 (2001).
- [12] M. Majumder and B. Corry, Anomalous decline of water transport in covalently modified carbon nanotube membranes, *Chem. Commun.* **47**, 7683 (2011).
- [13] Y. Baek, C. Kim, D. K. Seo, T. Kim, J. S. Lee, Y. H. Kim, K. H. Ahn, S. S. Bae, S. C. Lee, and J. Lim *et al.*, High performance and antifouling vertically aligned carbon nanotube membrane for water purification, *J. Membr. Sci.* **460**, 171 (2014).
- [14] M. Majumder, N. Chopra, and B. J. Hinds, Mass transport through carbon nanotube membranes in three different regimes: Ionic diffusion and gas and liquid flow, *ACS Nano* **5**, 3867 (2011).
- [15] F. Du, L. Qu, Z. Xia, L. Feng, and L. Dai, Membranes of vertically aligned superlong carbon nanotubes, *Langmuir* **27**, 8437 (2011).
- [16] B. Lee, Y. Baek, M. Lee, D. H. Jeong, H. H. Lee, J. Yoon, and Y. H. Kim, A carbon nanotube wall membrane for water treatment, *Nat. Commun.* **6**, 7109 (2015).
- [17] L. Zhang, B. Zhao, C. Jiang, J. Yang, and G. Zheng, Preparation and transport performances of high-density, aligned carbon nanotube membranes, *Nanoscale Res. Lett.* **10**, 266 (2015).
- [18] J. A. Thomas and A. J. McGaughey, Reassessing fast water transport through carbon nanotubes, *Nano Lett.* **8**, 2788 (2008).
- [19] K. Falk, F. Sedlmeier, L. Joly, R. R. Netz, and L. Bocquet, Molecular origin of fast water transport in carbon nanotube membranes: Superlubricity versus curvature dependent friction, *Nano Lett.* **10**, 4067 (2010).
- [20] J. A. Thomas, A. J. McGaughey, and O. Kuter-Arnebeck, Pressure-driven water flow through carbon nanotubes: Insights from molecular dynamics simulation, *Int. J. Thermal sci.* **49**, 281 (2010).
- [21] M. Suk, A. Raghunathan, and N. R. Aluru, Fast reverse osmosis using boron nitride and carbon nanotubes, *Appl. Phys. Lett.* **92**, 133120 (2008).
- [22] T. A. Hilder, D. Gordon, and S.-H. Chung, Salt rejection and water transport through boron nitride nanotubes, *Small* **5**, 2183 (2009).
- [23] G. Tocci, L. Joly, and A. Michaelides, Friction of water on graphene and hexagonal boron nitride from ab initio methods: Very different slippage despite very similar interface structures, *Nano Lett.* **14**, 6872 (2014).

- [24] S. Joseph and N. Aluru, Why are carbon nanotubes fast transporters of water?, *Nano Lett.* **8**, 452 (2008).
- [25] S. K. Kannam, P. J. Daivis, and B. Todd, Modeling slip and flow enhancement of water in carbon nanotubes, *MRS Bulletin* **42**, 283 (2017).
- [26] J. Israelachvili and R. Pashley, The hydrophobic interaction is long range, decaying exponentially with distance, *Nature* **300**, 341 (1982).
- [27] E. E. Meyer, K. J. Rosenberg, and J. Israelachvili, Recent progress in understanding hydrophobic interactions, *Proc. Natl. Acad. Sci.* **103**, 15739 (2006).
- [28] S. H. Donaldson Jr, A. Røyne, K. Kristiansen, M. V. Rapp, S. Das, M. A. Gebbie, D. W. Lee, P. Stock, M. Valtiner, and J. Israelachvili, Developing a general interaction potential for hydrophobic and hydrophilic interactions, *Langmuir* **31**, 2051 (2014).
- [29] K. Wu, Z. Chen, J. Li, X. Li, J. Xu, and X. Dong, Wettability effect on nanoconfined water flow, *Proc. Natl. Acad. Sci.* **114**, 3358 (2017).
- [30] M. Shaat and Y. Zheng, Fluidity and phase transitions of water in hydrophobic and hydrophilic nanotubes, *Sci. Rep.* **9**, 5689 (2019).
- [31] J. N. Israelachvili, *Intermolecular and Surface Forces* (Elsevier Science & Technology, Saint Louis, 2010).
- [32] F. Leroy, S. Liu, and J. Zhang, Parametrizing nonbonded interactions from wetting experiments via the work of adhesion: Example of water on graphene surfaces, *J. Phys. Chem. C* **119**, 28470 (2015).
- [33] C.-J. Shih, Q. H. Wang, S. Lin, K.-C. Park, Z. Jin, M. S. Strano, and D. Blankshtein, Breakdown in the Wetting Transparency of Graphene, *Phys. Rev. Lett.* **109**, 176101 (2012).
- [34] C. D. van Engers, N. E. Cousens, V. Babenko, J. Britton, B. Zappone, N. Grobert, and S. Perkin, Direct measurement of the surface energy of graphene, *Nano Lett.* **17**, 3815 (2017).
- [35] J. Rafiee, X. Mi, H. Gullapalli, A. V. Thomas, F. Yavari, Y. Shi, P. M. Ajayan, and N. A. Koratkar, Wetting transparency of graphene, *Nat. Mater.* **11**, 217 (2012).
- [36] A. Kozbial, Z. Li, C. Conaway, R. McGinley, S. Dhingra, V. Vahdat, F. Zhou, B. D'Urso, H. Liu, and L. Li, Study on the surface energy of graphene by contact angle measurements, *Langmuir* **30**, 8598 (2014).
- [37] P.-C. Ma, S.-Y. Mo, B.-Z. Tang, and J.-K. Kim, Dispersion, interfacial interaction and re-agglomeration of functionalized carbon nanotubes in epoxy composites, *Carbon* **48**, 1824 (2010).
- [38] M. Heiranian and N. R. Aluru, Nanofluidic transport theory with enhancement factors approaching one, *ACS Nano* **14**, 272 (2019).
- [39] W. Sparreboom, A. van den Berg, and J. C. Eijkel, Principles and applications of nanofluidic transport, *Nat. Nanotechnol.* **4**, 713 (2009).
- [40] L. Bocquet and E. Charlaix, Nanofluidics, from bulk to interfaces, *Chem. Soc. Rev.* **39**, 1073 (2010).
- [41] M. Aminpour, S. Galindo-Torres, A. Scheuermann, and L. Li, Pore-Scale Behavior of Darcy Flow in Static and Dynamic Porous Media, *Phys. Rev. Appl.* **9**, 064025 (2018).
- [42] M. Aminpour, S. Galindo-Torres, A. Scheuermann, and L. Li, Slip-flow lattice-boltzmann simulations in ducts and porous media: A full rehabilitation of spurious velocities, *Phys. Rev. E* **98**, 043110 (2018).
- [43] C. J. Van Oss, *Interfacial Forces in Aqueous Media* (CRC Press, Boca Raton, 2006), 2nd ed.
- [44] C. J. Van Oss, M. K. Chaudhury, and R. J. Good, Interfacial lifshitz-van der waals and polar interactions in macroscopic systems, *Chem. Rev.* **88**, 927 (1988).
- [45] S. Wang, Y. Zhang, N. Abidi, and L. Cabrales, Wettability and surface free energy of graphene films, *Langmuir* **25**, 11078 (2009).
- [46] T. Dreher, C. Lemarchand, N. Pineau, E. Bourasseau, A. Ghoufi, and P. Malfreyt, Calculation of the interfacial tension of the graphene-water interaction by molecular simulations, *J. Chem. Phys.* **150**, 014703 (2019).
- [47] K. Ritos, D. Mattia, F. Calabrò, and J. M. Reese, Flow enhancement in nanotubes of different materials and lengths, *J. Chem. Phys.* **140**, 014702 (2014).
- [48] T. Huhtamäki, X. Tian, J. T. Korhonen, and R. H. Ras, Surface-wetting characterization using contact-angle measurements, *Nat. Protoc.* **13**, 1521 (2018).
- [49] T. A. Ho, D. V. Papavassiliou, L. L. Lee, and A. Striolo, Liquid water can slip on a hydrophilic surface, *Proc. Natl. Acad. Sci.* **108**, 16170 (2011).
- [50] J. Janecek and R. R. Netz, Interfacial water at hydrophobic and hydrophilic surfaces: Depletion versus adsorption, *Langmuir* **23**, 8417 (2007).
- [51] C. Sendner, D. Horinek, L. Bocquet, and R. R. Netz, Interfacial water at hydrophobic and hydrophilic surfaces: Slip, viscosity, and diffusion, *Langmuir* **25**, 10768 (2009).
- [52] A. Poynor, L. Hong, I. K. Robinson, S. Granick, Z. Zhang, and P. A. Fenter, How Water Meets a Hydrophobic Surface, *Phys. Rev. Lett.* **97**, 266101 (2006).
- [53] M. Mezger, H. Reichert, S. Schöder, J. Okasinski, H. Schröder, H. Dosch, D. Palms, J. Ralston, and V. Honkimäki, High-resolution in situ *x*-ray study of the hydrophobic gap at the water–octadecyl-trichlorosilane interface, *Proc. Natl. Acad. Sci.* **103**, 18401 (2006).
- [54] B. Todd, J. Hansen, and P. J. Daivis, Nonlocal Shear Stress for Homogeneous Fluids, *Phys. Rev. Lett.* **100**, 195901 (2008).
- [55] P.-A. Mante, C.-C. Chen, Y.-C. Wen, H.-Y. Chen, S.-C. Yang, Y.-R. Huang, I.-J. Chen, Y.-W. Chen, V. Gusev, and M.-J. Chen *et al.*, Probing hydrophilic interface of solid/liquid-water by nanoultrasonics, *Sci. Rep.* **4**, 6249 (2014).
- [56] K. Yum and M.-F. Yu, Measurement of wetting properties of individual boron nitride nanotubes with the wilhelmy method using a nanotube-based force sensor, *Nano Lett.* **6**, 329 (2006).
- [57] A. Ammar, A. Elzatahry, M. Al-Maadeed, A. M. Alenizi, A. F. Huq, and A. Karim, Nanoclay compatibilization of phase separated polysulfone/polyimide films for oxygen barrier, *Appl. Clay Sci.* **137**, 123 (2017).
- [58] A. S. Bhurke, P. A. Askeland, and L. T. Drzal, Surface modification of polycarbonate by ultraviolet radiation and ozone, *J. Adhes.* **83**, 43 (2007).

- [59] K. P. Travis, B. Todd, and D. J. Evans, Departure from navier-stokes hydrodynamics in confined liquids, *Phys. Rev. E* **55**, 4288 (1997).
- [60] A. Noy, H. G. Park, F. Fornasiero, J. K. Holt, C. P. Grigoropoulos, and O. Bakajin, Nanofluidics in carbon nanotubes, *Nano Today* **2**, 22 (2007).
- [61] X. Qin, Q. Yuan, Y. Zhao, S. Xie, and Z. Liu, Measurement of the rate of water translocation through carbon nanotubes, *Nano Lett.* **11**, 2173 (2011).
- [62] S. Sinha, M. Pia Rossi, D. Mattia, Y. Gogotsi, and H. H. Bau, Induction and measurement of minute flow rates through nanopipes, *Phys. Fluids* **19**, 013603 (2007).
- [63] S. Kim, F. Fornasiero, H. G. Park, J. B. In, E. Meshot, G. Giraldo, M. Stadermann, M. Fireman, J. Shan, and C. P. Grigoropoulos *et al.*, Fabrication of flexible, aligned carbon nanotube/polymer composite membranes by in-situ polymerization, *J. Membrane Sci.* **460**, 91 (2014).
- [64] N. Bui, E. R. Meshot, S. Kim, J. Peña, P. W. Gibson, K. J. Wu, and F. Fornasiero, Ultrabreathable and protective membranes with sub-5 nm carbon nanotube pores, *Adv. Mater.* **28**, 5871 (2016).
- [65] M. Yu, H. H. Funke, J. L. Falconer, and R. D. Noble, High density, vertically-aligned carbon nanotube membranes, *Nano Lett.* **9**, 225 (2009).
- [66] R. L. McGinnis, K. Reimund, J. Ren, L. Xia, M. R. Chowdhury, X. Sun, M. Abril, J. D. Moon, M. M. Merrick, and J. Park *et al.*, Large-scale polymeric carbon nanotube membranes with sub-1.27-nm pores, *Sci. Adv.* **4**, e1700938 (2018).
- [67] N. Kavokine, R. R. Netz, and L. Bocquet, Fluids at the nanoscale: From continuum to subcontinuum transport, *Annu. Rev. Fluid Mech.* **53**, 377 (2021).
- [68] T. B. Sisan and S. Lichter, The end of nanochannels, *Microfluid. Nanofluidics* **11**, 787 (2011).
- [69] J. S. Babu and S. P. Sathian, The role of activation energy and reduced viscosity on the enhancement of water flow through carbon nanotubes, *J. Chem. Phys.* **134**, 194509 (2011).
- [70] W. Nicholls, M. K. Borg, D. A. Lockerby, and J. Reese, Water transport through carbon nanotubes with defects, *Mol. Simul.* **38**, 781 (2012).
- [71] S. K. Kannam, B. Todd, J. S. Hansen, and P. J. Davis, How fast does water flow in carbon nanotubes?, *J. Chem. Phys.* **138**, 094701 (2013).
- [72] J. R. Bordin, A. Diehl, and M. C. Barbosa, Relation between flow enhancement factor and structure for core-softened fluids inside nanotubes, *J. Phys. Chem. B* **117**, 7047 (2013).
- [73] J. H. Walther, K. Ritos, E. R. Cruz-Chu, C. M. Megaridis, and P. Koumoutsakos, Barriers to superfast water transport in carbon nanotube membranes, *Nano Lett.* **13**, 1910 (2013).
- [74] J. Tao, X. Song, T. Zhao, S. Zhao, and H. Liu, Confinement effect on water transport in cnt membranes, *Chem. Eng. Sci.* **192**, 1252 (2018).
- [75] A. Sam, V. Prasad, and S. P. Sathian, Water flow in carbon nanotubes: The role of tube chirality, *Phys. Chem. Chem. Phys.* **21**, 6566 (2019).
- [76] S. Casanova, M. K. Borg, Y. J. Chew, and D. Mattia, Surface-controlled water flow in nanotube membranes, *ACS Appl. Mater. Interfaces* **11**, 1689 (2018).
- [77] T. Werder, J. H. Walther, R. Jaffe, T. Halicioglu, and P. Koumoutsakos, On the water-carbon interaction for use in molecular dynamics simulations of graphite and carbon nanotubes, *J. Phys. Chem. B* **107**, 1345 (2003).
- [78] E. Bonaccorso, M. Kappl, and H.-J. Butt, Hydrodynamic Force Measurements: Boundary Slip of Water on Hydrophilic Surfaces and Electrokinetic Effects, *Phys. Rev. Lett.* **88**, 076103 (2002).
- [79] K. P. Lee, H. Leese, and D. Mattia, Water flow enhancement in hydrophilic nanochannels, *Nanoscale* **4**, 2621 (2012).
- [80] R. H. Tunuguntla, R. Y. Henley, Y.-C. Yao, T. A. Pham, M. Wanunu, and A. Noy, Enhanced water permeability and tunable ion selectivity in subnanometer carbon nanotube porins, *Science* **357**, 792 (2017).
- [81] M. H. Köhler, J. R. Bordin, C. F. de Matos, and M. C. Barbosa, Water in nanotubes: The surface effect, *Chem. Eng. Sci.* **203**, 54 (2019).
- [82] H. Wang, Z. Huang, Q. Cai, K. Kulkarni, C.-L. Chen, D. Carnahan, and Z. Ren, Reversible transformation of hydrophobicity and hydrophilicity of aligned carbon nanotube arrays and buckypapers by dry processes, *Carbon* **48**, 868 (2010).
- [83] S. Succi, A. Mohammad, and J. Horbach, Lattice-boltzmann simulation of dense nanoflows: A comparison with molecular dynamics and navier-stokes solutions, *Int. J. Mod. Phys. C* **18**, 667 (2007).
- [84] R. Qiao and N. Aluru, Ion concentrations and velocity profiles in nanochannel electroosmotic flows, *J. Chem. Phys.* **118**, 4692 (2003).
- [85] W. Sparreboom, A. van den Berg, and J. C. Eijkel, Transport in nanofluidic systems: A review of theory and applications, *New J. Phys.* **12**, 015004 (2010).
- [86] A. F. Brandner, S. Timr, S. Melchionna, P. Derreumaux, M. Baaden, and F. Sterpone, Modelling lipid systems in fluid with lattice boltzmann molecular dynamics simulations and hydrodynamics, *Sci. Rep.* **9**, 1 (2019).
- [87] F. Sterpone, P. Derreumaux, and S. Melchionna, Protein simulations in fluids: Coupling the opep coarse-grained force field with hydrodynamics, *J. Chem. Theory Comput.* **11**, 1843 (2015).
- [88] M. Chiricotto, S. Melchionna, P. Derreumaux, and F. Sterpone, Hydrodynamic effects on β -amyloid (16-22) peptide aggregation, *J. Chem. Phys.* **145**, 035102 (2016).
- [89] X. He and L.-S. Luo, Lattice boltzmann model for the incompressible navier-stokes equation, *J. Stat. Phys.* **88**, 927 (1997).
- [90] C. K. Aidun and J. R. Clausen, Lattice-boltzmann method for complex flows, *Annu. Rev. Fluid Mech.* **42**, 439 (2010).
- [91] X. He, X. Shan, and G. D. Doolen, Discrete boltzmann equation model for nonideal gases, *Phys. Rev. E* **57**, R13 (1998).
- [92] M. L. Porter, E. Coon, Q. Kang, J. Moulton, and J. Carey, Multicomponent interparticle-potential lattice boltzmann model for fluids with large viscosity ratios, *Phys. Rev. E* **86**, 036701 (2012).

- [93] X. He, S. Chen, and G. D. Doolen, A novel thermal model for the lattice boltzmann method in incompressible limit, *J. Comput. Phys.* **146**, 282 (1998).
- [94] J. S. Rowlinson and B. Widom, *Molecular Theory of Capillarity* (Courier Corporation, Mineola, New York, 2013).
- [95] D. Lycett-Brown and K. H. Luo, Improved forcing scheme in pseudopotential lattice boltzmann methods for multiphase flow at arbitrarily high density ratios, *Phys. Rev. E* **91**, 023305 (2015).
- [96] R. Raj, S. C. Maroo, and E. N. Wang, Wettability of graphene, *Nano Lett.* **13**, 1509 (2013).
- [97] Y. J. Shin, Y. Wang, H. Huang, G. Kalon, A. T. S. Wee, Z. Shen, C. S. Bhatia, and H. Yang, Surface-energy engineering of graphene, *Langmuir* **26**, 3798 (2010).
- [98] S. Nuriel, L. Liu, A. Barber, and H. Wagner, Direct measurement of multiwall nanotube surface tension, *Chem. Phys. Lett.* **404**, 263 (2005).
- [99] S. C. Roh, E. Y. Choi, Y. S. Choi, and C. Kim, Characterization of the surface energies of functionalized multiwalled carbon nanotubes and their interfacial adhesion energies with various polymers, *Polymer* **55**, 1527 (2014).
- [100] N. Rathod and S. G. Hatzikiriakos, The effect of surface energy of boron nitride on polymer processability, *Polymer Eng. Sci.* **44**, 1543 (2004).
- [101] A. Ponter, W. Jones Jr, and R. Jansen, Surface energy changes produced by ultraviolet-ozone irradiation of poly (methyl methacrylate), polycarbonate, and polytetrafluoroethylene, *Polymer Eng. Sci.* **34**, 1233 (1994).
- [102] K. Kim, K. Lee, K. Cho, and C. Park, Surface modification of polysulfone ultrafiltration membrane by oxygen plasma treatment, *J. Membr. Sci.* **199**, 135 (2002).
- [103] Y.-Q. Song, J. Sheng, M. Wei, and X.-B. Yuan, Surface modification of polysulfone membranes by low-temperature plasma-graft poly (ethylene glycol) onto polysulfone membranes, *J. Appl. Polym. Sci.* **78**, 979 (2000).
- [104] M. P. Goertz, J. Houston, and X.-Y. Zhu, Hydrophilicity and the viscosity of interfacial water, *Langmuir* **23**, 5491 (2007).
- [105] U. Raviv, P. Laurat, and J. Klein, Fluidity of water confined to subnanometre films, *Nature* **413**, 51 (2001).
- [106] M. Neek-Amal, F. M. Peeters, I. V. Grigorieva, and A. K. Geim, Commensurability effects in viscosity of nanoconfined water, *ACS Nano* **10**, 3685 (2016).
- [107] M. U. Hammer, T. H. Anderson, A. Chaimovich, M. S. Shell, and J. Israelachvili, The search for the hydrophobic force law, *Faraday Discuss.* **146**, 299 (2010).
- [108] R. F. Tabor, C. Wu, F. Grieser, R. R. Dagastine, and D. Y. Chan, Measurement of the hydrophobic force in a soft matter system, *J. Phys. Chem. Lett.* **4**, 3872 (2013).
- [109] P. Stock, T. Utzig, and M. Valtiner, Direct and quantitative afm measurements of the concentration and temperature dependence of the hydrophobic force law at nanoscopic contacts, *J. Colloid Interface Sci.* **446**, 244 (2015).
- [110] A. Alexiadis, and S. Kassinos, Self-diffusivity, hydrogen bonding and density of different water models in carbon nanotubes, *Mol. Simul.* **34**, 671 (2008).
- [111] A. Alexiadis and S. Kassinos, The density of water in carbon nanotubes, *Chem. Eng. Sci.* **63**, 2047 (2008).
- [112] A. Alexiadis and S. Kassinos, Molecular simulation of water in carbon nanotubes, *Chem. Rev.* **108**, 5014 (2008).
- [113] L. Chen, Q. Kang, Y. Mu, Y.-L. He, and W.-Q. Tao, A critical review of the pseudopotential multiphase lattice boltzmann model: Methods and applications, *Int. J. Heat Mass Transf.* **76**, 210 (2014).
- [114] J. Harting, C. Kunert, and H. J. Herrmann, Lattice boltzmann simulations of apparent slip in hydrophobic microchannels, *EPL (Europhysics Letters)* **75**, 328 (2006).
- [115] R. Benzi, L. Biferale, M. Sbragaglia, S. Succi, and F. Toschi, Mesoscopic two-phase model for describing apparent slip in micro-channel flows, *EPL (Europhysics Letters)* **74**, 651 (2006).
- [116] L. Zhu, D. Trethewey, L. Petzold, and C. Meinhart, Simulation of fluid slip at 3d hydrophobic microchannel walls by the lattice boltzmann method, *J. Comput. Phys.* **202**, 181 (2005).
- [117] J. Harting, C. Kunert, and J. Hyväluoma, Lattice boltzmann simulations in microfluidics: Probing the no-slip boundary condition in hydrophobic, rough, and surface nanobubble laden microchannels, *Microfluidics Nanofluidics* **8**, 1 (2010).
- [118] B. Halperin, *Progress in low Temperature Physics* (Elsevier, 2005), Vol. 15.